# ASTER Data Analysis Applied to Mineral Resource Exploration and Geological Mapping

# （ASTER データ解析の鉱物資源探査及び地質マッピングへの適用）

YAJIMA, Taro

（矢島　太郎）

# ASTER Data Analysis Applied to Mineral Resource Exploration and Geological Mapping

# （ASTER データ解析の鉱物資源探査及び地質マッピングへの適用）

YAJIMA, Taro

（矢島　太郎）

A dissertation for the degree of Doctor of Science
Department of Earth and Environmental Sciences,
Graduate School of Environmental Studies, Nagoya University
（名古屋大学大学院環境学研究科地球環境科学専攻学位論文　博士（理学））

2014

# CONTENTS

## List of Figures

## List of Tables

# SUMMARY

Spaceborne remote sensing sensors are able to provide global information of the earth's surface and important data for evaluation of regional areas for mineral resources exploration in the early stage. Identification of alteration zones and alteration mineralogy is important for exploration of porphyry copper deposits which is a major copper deposit type that provides more than 50 % of copper supply. Geological mapping and identification of mafic to ultramafic units is important for exploration of magmatic deposits which provide most of nickel and platinum group elements.

Advanced Spaceborne Thermal Emission and Reflection Radiometer (ASTER) is a Japanese satelliteborne optical sensor equipped with 14 bands from the visible to near infrared (VNIR), shortwave infrared (SWIR) and thermal infrared (TIR) wavelength regions. Digital elevation model (DEM) data is created from the stereo band 3N and 3B and provided as ASTER Global DEM (GDEM) data. This thesis describes the processing methods and applications of ASTER data for mineral resources exploration and geological mapping in three sections; (1) alteration mapping using ASTER VNIR and SWIR data, (2) geological mapping using ASTER TIR data, and (3) geological mapping using ASTER GDEM data.

(1) Alteration mapping using ASTER VNIR and SWIR data

Alteration zones are important features for the exploration of porphyry copper deposits and the ASTER sensor is able to identify the type of alteration and its alteration zoning. Here, the combined utilization of the following three specific images created from ASTER data for this purpose is described: 1) a SWIR false color image, 2) band ratio color composite image, and 3) a principal component analysis (PCA) color composite image.

The SWIR false color image is a false color image using bands 4, 6 and 8 (R:G:B= 4:6:8). The alteration zones appear as pink or green in the image.

The band ratio color composite image uses the band ratio images of band 4/band 6, band 5/band 6 and band 5/band 8 (R:G:B=4/6:5/6:5/8). The band ratio image is able to provide information on the alteration zoning. Band 4/band 6 enhances the advanced argillic alteration, band 5/band 6 enhances the phyllic alteration and band 5/band 8 enhances the propylitic alteration.

The PCA image ("Crosta technique") is also able to provide information on the alteration zoning. The PCA color composite image consists of PCA alteration images obtained from three PCA processes (R:G:B=PCA advanced argillic alteration image:

PCA phyllic alteration image: PCA propylitic alteration image). The advanced argillic alteration image is obtained from PCA of bands 1, 4, 6 and 7, the phyllic alteration image from PCA of bands 1, 3, 5 and 6 and the propylitic alteration image from PCA of band 1, 3, 5 and 8. The PCA alteration images are chosen by checking the eigenvectors.

These methods are applied to the Meiduk area of Iran, which is known for porphyry copper mineralizations. We found that combinational use of the images enables successful identification of the hydrothermal alteration and zonings related to porphyry copper mineralization.

(2) Geological mapping using ASTER TIR data

Geological units are identified by using ASTER TIR data, which contains both surface temperature and spectral emissivity information. In ASTER L1B day time TIR data, bands 10, 11, and 12 contain spectral emissivity and temperature information, whereas surface temperature dominates the spectral emissivity information in bands 13 and 14. Visual interpretation of the ASTER TIR false color images generated by assigning band 14, band 12 and band 10 (R:G:B=band 14:band 12:band 10) using L1B day time data allowed to identify mafic-to-ultramafic units and quartz-rich felsic units. Mafic-to-ultramafic units such as gabbro, dolerite, and dunite appear white in ASTER L1B day time TIR false color images due to their high spectral emissivities and high surface temperatures. Mafic-to-ultramafic units have higher surface temperatures than other geological units because they absorb more solar radiation due to their lower albedos. Quartz-rich felsic units such as granite and dry river sand appear reddish in the ASTER L1B day time TIR false color image because the spectral emissivity of quartz. Mafic-to-ultramafic and granitic units are important targets for mineral exploration because they are potential geological units to host or accompany mineralization.

(3) Geological mapping using ASTER GDEM data

Inverted slope images created from DEMs can be used to visualize differences in lithological units and provide an indication of areas of geological outcropping. Such images are useful for geological mapping, but when created from DEMs generated from remote sensing images (“image-derived DEMs”), artifacts in the DEMs are exaggerated and give rise to unclear noisy final images. In contrast, DEMs created from elevation data in the form of contour maps (“contour-derived DEMs”) contain far fewer artifacts, but their availability is limited. Therefore, in order to obtain clear processed DEM images that can be used for global geological mapping, it is necessary to develop a method for reducing the number of artifacts in image-derived DEMs.

The effectiveness of a fast Fourier transform (FFT) for artifact reduction in image-derived DEMs was investigated. It was clarified that for the image-derived DEMs, that a low-pass filter with a size of 20 to 40 % significantly reduced the number of artifacts without significant loss of terrain information. For the ASTER GDEM data, artifact reduction was found to be particularly important because the artifacts obscure the original topographic information in the inverted slope images.

The proposed methods in this study are simple but useful and provide reproducible results. The images could be used widely by geologists or geophysicists involved in mineral resources exploration. ASTER VNIR and SWIR data have been widely used in exploration for alteration mapping mainly targeting hydrothermal ore deposits that accompany alteration minerals, and this study has also considered the ability of ASTER TIR and GDEM data for use in geological mapping and its effectiveness for exploration of magmatic ore deposits.

# CHAPTER 1

## Introduction

### 1.1 Target ore deposit types for mineral resources exploration

#### 1.1.1 Hydrothermal ore deposits

Hydrothermal ore deposits are created by the activity of fertile fluids that are rich in metals. Hydrothermal fluids consist of magmatic intrusion origin water and meteoric water in various proportions. Precipitation of the metals in the hydrothermal fluid is triggered by change or fluctuation of the fluid condition (mixing, cooling, boiling, etc.). Porphyry copper type deposits (Cu±Au±Mo), epithermal auriferous vein type deposits (Au-Ag), subepithermal polymetallic vein type deposits (Zn-Cu-Pb-Ag±Au), and skarn type deposits (Zn-Pb), are examples of hydrothermal ore deposits created in different geological and spatial situations from the multiphase porphyry stock (Sillitoe, 2010) (Figure 1.1).

Hydrothermal alteration is created simultaneously with the hydrothermal mineralization process. Porphyry copper type deposits are accompanied by extreme hydrothermal alteration surrounding the ore deposit over many cubic kilometers. Zoned alteration is created depending on the temperature and chemical condition of the fluid (Sillitoe, 2010) (Figure 1.2).

#### 1.1.2 Magmatic ore deposits

Magmatic ore deposits are created within specific magmatic intrusions. Mafic to ultramafic intrusions host mineralization of metals such as nickel, copper and platinum group elements (PGE). Mineralization occurs within the mafic to ultramafic intrusion (Figure 1.3 (c), Figure 1.4) and also in the feeder dykes (Barnes and Lightfoot, 2005; Naldrett, 2004). Precipitation of the sulfides in the magma is triggered by the feed of sulfur caused by contamination of the sulfur rich sedimentary host rock with mafic magma (Figure 1.3 (a)). Nickel, copper, and PGE in the magma create sulfides and settle at the base of the magma (Figure 1.3 (b)). Nickel sulfide deposits (Ni-Cu-PGE) and PGE deposits are typical magmatic ore deposits that are related to mafic to ultramafic magmas.

### 1.2 ASTER sensor

The Advanced Spaceborne Thermal Emission and Reflection Radiometer (ASTER) is a multiband optical scanner on board NASA's TERRA platform that was launched in

December 1999. ASTER was designed by NASA and Japan's Ministry of Economy Trade and Industry (METI) as a next generation remote sensing sensor for earth observation following Landsat and JERS-1. ASTER provides optical data in 14 spectral bands: 3 bands from the visible to near infrared (VNIR), 6 bands from the shortwave infrared (SWIR) and 5 bands from the thermal infrared (TIR) wavelength regions (Figure 1.5). ASTER also obtains stereo data at band 3 (band 3N (nadir) and band 3B (backward)) for digital elevation model creation (Figure 1.6). The ASTER Global DEM (GDEM) was released on June 2009 and covers most of the earth's surface and the updated GDEM2 was released on October 2011.

ASTER is designed with capabilities to identify minerals and geology using VNIR, SWIR, TIR and GDEM data. Processing methods applicable for mineral exploration and geological mapping using VNIR, SWIR, TIR and GDEM data needs to be investigated and have been studied in this thesis.

## 1.3 Exploration targets for ASTER

Zoned alterations are important targets for exploration of hydrothermal ore deposits because alteration created by weathering effects usually does not display zoned alteration. ASTER data processing methods to identify hydrothermal alteration and to clarify the zoned alteration are needed.

Identification of mafic to ultramafic units from remote sensing data is important for exploration of nickel sulfide deposits and PGE deposits. ASTER data processing methods for geological mapping and identification of mafic to ultramafic units are also needed.

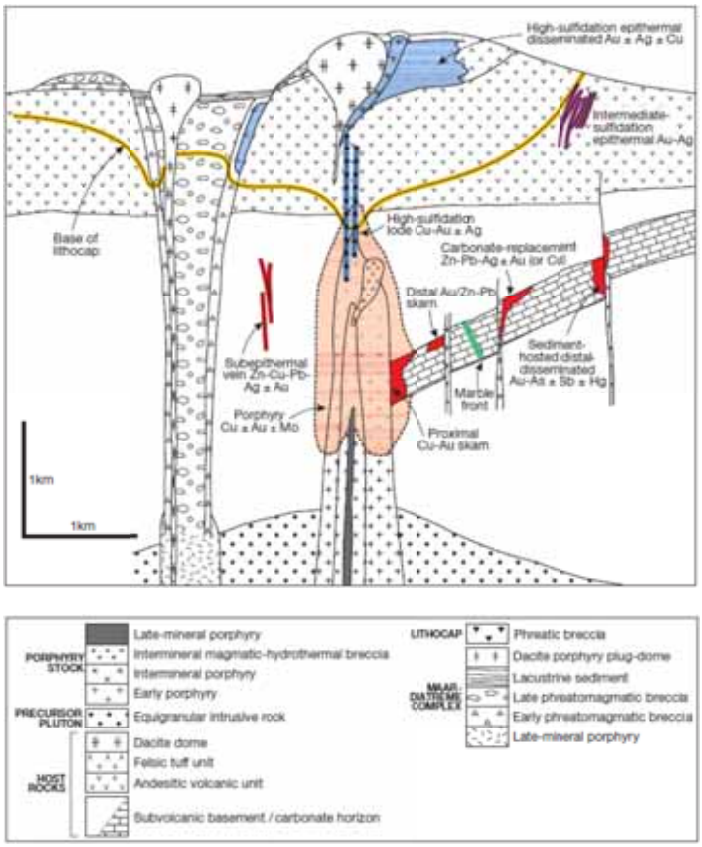


Figure 1.1 Anatomy of a telescoped porphyry Cu system (Sillitoe, 2010).

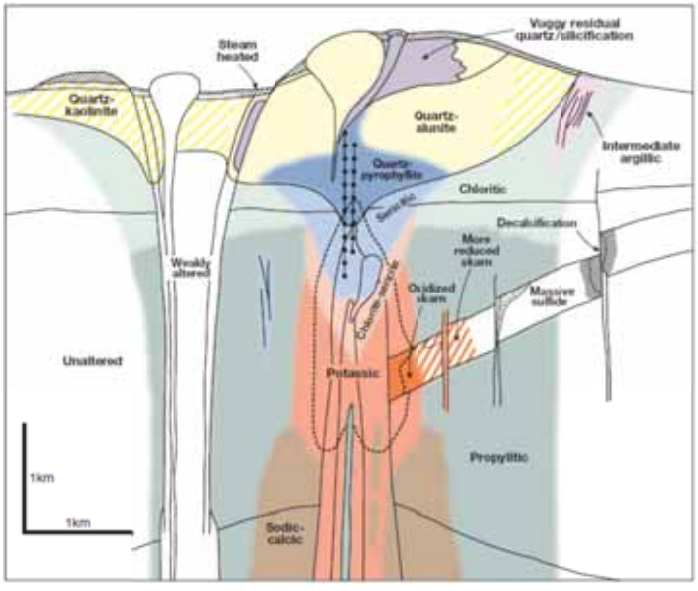


Figure 1.2 Generalized alteration-mineralization zoning pattern for telescoped porphyry Cu deposits (Sillitoe, 2010).

(a) Contamination of the mafic magma brings about sulfide from S-rich country rock sediments

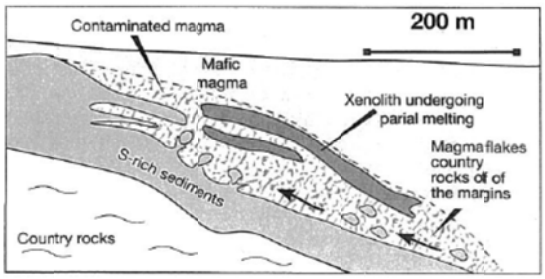


(b) Collection of the sulfides in some structural trap

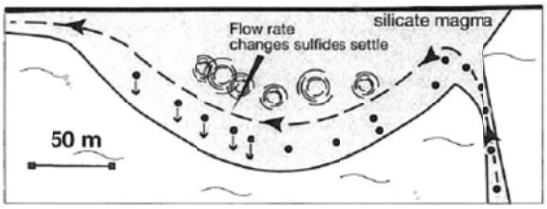


(c) Crystallization of sulfide liquid creates massive sulfide rich cumulate

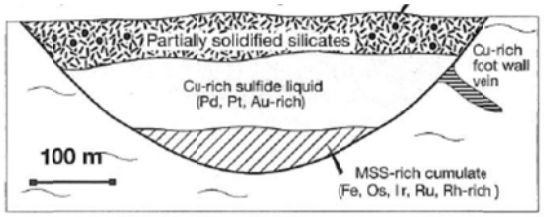


Figure 1.3 Formation process of a magmatic Ni sulfide ore deposit (Barnes and Lightfoot, 2005).

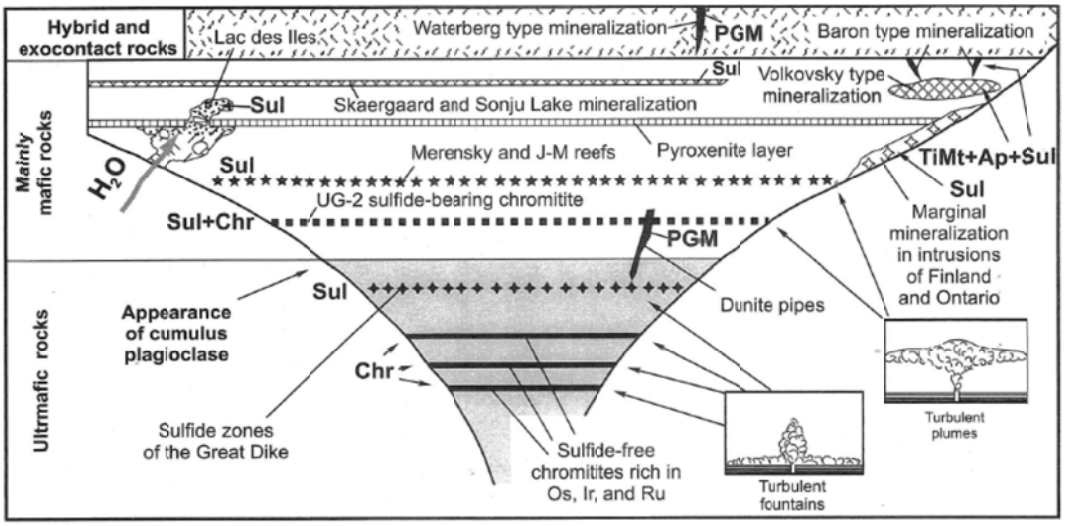


Figure 1.4 Model cross-section through a hypothetical layered intrusion, showing different types of PGE deposits (Naldrett, 2004).

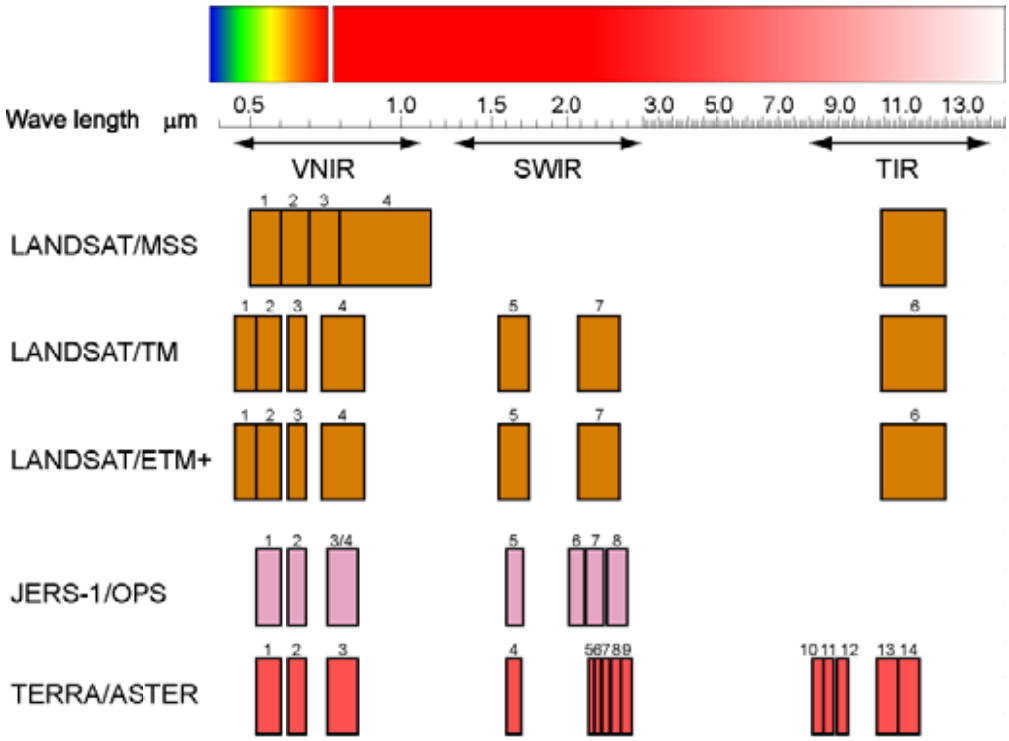


Figure 1.5 Band configurations of spaceborne optical sensors.

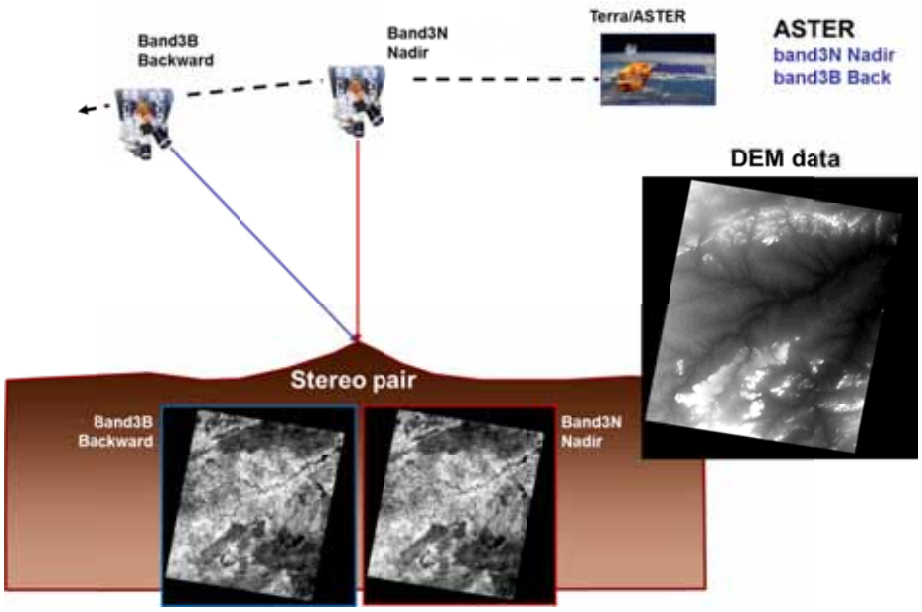


(TERRA/ASTER image copyright of Japan Space Systems and NASA)

Figure 1.6 ASTER DEM creation.

# CHAPTER 2

## Identification of hydrothermal alteration zones for exploration of porphyry copper deposits using ASTER data

### 2.1 Introduction

Remote sensing data have been used in mineral exploration since the launch of Landsat-1 in 1972. It has mainly been used for identification of alteration zones and geological mapping. Japan has developed the JERS-1 (Japanese Earth Resources Satellite-1) for mineral exploration and the ASTER (Advanced Spaceborne Thermal Emission and Reflection Radiometer) sensor that has been also designed for mineral exploration, but data processing methods for mineral exploration using ASTER have not been clarified since its launch in 1999. Here we develop simple and robust processing methods to identify hydrothermal alteration and alteration zonings using ASTER data for the exploration of porphyry copper deposits through research of exploration programs conducted by the Japan Oil, Gas and Metals National Corporation (JOGMEC).

### 2.2 Hydrothermal alteration and alteration minerals

Porphyry copper deposits are low in ore grade (0.3 to 1.0 % Cu), but create a large scale ore deposit that can be developed by low cost open pit mining. More than 50 % of the world's copper is presently produced from porphyry copper deposits. Porphyry copper deposits are created by granodioritic intrusions that intruded into the shallow crust. Granodioritic intrusions are accompanied by hydrothermal fluid, which creates the porphyry copper deposit and distinct hydrothermal alteration of the surrounding host rocks.

The hydrothermal fluid creates the ore deposit and also hydrothermal alteration is developed in the host rocks surrounding the ore deposit, and thus the alteration zone is an important feature for mineral exploration. Different characteristics of the hydrothermal fluid such as temperature, fluid/rock ratio and also the chemical difference of the host rock produce diverse alteration minerals. This causes the development of alteration zoning and provides important information on the hydrothermal fluid and for exploration. The location of the ore deposit and ore deposit type can be estimated from the alteration mineralogy and by the mode of occurrence of the alteration zoning.

A typical alteration zoning related to porphyry copper deposits consists of a granodioritic intrusion at the center accompanied by a potassic alteration (K feldspar

and biotite), phyllic alteration (sericite and quartz), and propylitic alteration (chlorite, epidote, calcite, etc.) moving outwards (Sillitoe, 2000). Also, when the deposit is hidden underground, an advanced argillic alteration (alunite and kaolinite) is created at the surface on the top of the deposit (Figure 2.1). Copper ore is generally distributed in the central region of the alteration zoning (potassic to phyllic alteration) where the hydrothermal fluid has high temperature.

Alteration minerals that create alteration zoning have characteristic absorption patterns (Figure 2.2), especially in the short wave infrared (SWIR) region (2.0 to 2.5 μm). Remote sensing used in mineral exploration of hydrothermal ore deposits often use the spectral features of the alteration minerals at wavelength of 2.0 to 2.5 μm to find alteration zones and identify alteration minerals. Landsat only has one band (band 7) for observation in the wavelength region 2.0 to 2.5 μm and only can determine the presence of alteration, but ASTER has five bands in this region and is able to identify not only the presence of alteration, but differentiate the minerals in the alteration zone (Table 2.1).

Alunite and kaolinite, which are alteration minerals present in advanced argillic alteration, have absorptions at 2.16 μm and 2.2 μm that are created by the aluminum hydroxyl (Al-OH) bond (Figure 2.2 left). Sericite, which is a typical alteration mineral in phyllic alteration, has an absorption at 2.2 μm that is also created by the Al-OH bond. Chlorite, epidote and calcite, which are present in propylitic alteration, have an absorption at 2.35 μm that is created by the magnesium hydroxyl (Mg-OH) bond and the carbonic ($CO_3$) bond. These alteration minerals can be identified by ASTER's five spectral bands in the wavelengths of 2.0 to 2.5 μm (Figure 2.2 right), but the potassic alteration that is located at the center of the alteration zoning of the porphyry copper deposit could not be identified from the spectral pattern of the visible near infrared (VNIR) to SWIR because K feldspar and biotite does not have a characteristic absorption in this wavelength region.

## 2.3 Study area

The Meiduk area located in the Kerman state of Iran is selected as the case study site because the area is associated with widespread hydrothermal alteration at the surface. The Meiduk area is located approximately 200 km west of the city of Kerman (Figure 2.3) and is a mountainous area with altitudes of 2,000 to 3,000 m. The northwest to southeast trending mountains from Western Yazd to the southern Kerman area that contains the Meiduk area was an active volcanic terrain in the Paleogene when many granodioritic intrusions occurred. Porphyry copper deposits, being vein type deposits of

Zn-Pb-$BaSO_4$, were created in the Kerman area (JOGMEC, 2005). The Meiduk porphyry copper deposit with an ore reserve of 145 Mt at 0.8 % Cu ore grade is located in the mountains of the Meiduk area. The deposit has an alteration zoning of potassic alteration, phyllic alteration, argillic alteration, then propylitic alteration from the center to the outer zones and silicification also accompanies the alteration (Tangestani and Moore, 2002). The Sarcheshmeh deposit, being the largest porphyry copper deposit in Iran, with an ore reserve of 1,250 Mt at 0.6 % Cu ore grade, is located approximately 100 km west of the city of Kerman. It is also present on the southeast elongation of the same northwest to southeast trending mountains from the Meiduk deposit (MMAJ, 2003).

### 2.4 ASTER data processing

Data processing methods such as false color images, band ratio images and principal component analysis (PCA) images using Landsat data for mineral exploration has already been introduced and established in past studies (Crippen, 1989; Crosta and Moore, 1989; Loughlin, 1991). In this study, we introduce effective false color images, band ratio images and PCA images using ASTER data for mineral exploration. Band ratio and PCA are simple data processing methods that are easily created and are reproducible.

For this study, we used ortho-corrected ASTER level 3A data (granule ID; AST3A1 030620070841041140426) and subset the image to an approximately 40 km by 45 km area containing the Meiduk deposit. We also used ASTER level 2 data, which are atmosphere corrected surface reflectance products (granule ID; AST2B5V 030620070841061010027 and AST2B5S 030620070841061010 0028), to compare with the data processing results obtained from the ASTER L3A data.

#### 2.4.1 Preprocessing of ASTER data

Preprocessing of ASTER data is necessary to obtain information on the slight difference of alteration minerals. Surface objects such as clouds, snow, ocean, lakes and the edges of the image need to be masked because these have significantly different spectral features to alteration minerals, and their removal allows visualization of the slight differences of alteration minerals in the alteration zone when applying band ratio or PCA. Areas with dense vegetation should also be masked for obtaining better alteration mineral identification because vegetation is sometimes identified as alteration when only SWIR bands are used for data processing and interpretation.

2.4.2 False color images

The SWIR false color image is useful for exploration of porphyry copper deposits because the main alteration accompanied with porphyry copper deposits are advanced argillic and phyllic alteration which are clearly visualized and enhanced in this image. SWIR false color images created by applying ASTER bands 4, 6, and 8 to red (R), green (G) and blue (B) (R:G:B=4:6:8) are useful for identification of alteration. In this SWIR false color image, advanced argillic alteration (alunite, kaolinite) and phyllic alteration (sericite, smectite) are indicated in red to pink, propylitic alteration (chlorite, epidote) is indicated in pale green and calcareous units are indicated in yellow. Advanced argillic and phyllic alteration both have absorption at band 6, low reflectance at band 8, high reflectance at band 4 (Figure 2.2) and appear as red to pink in the R:G:B=4:6:8 image. Propylite alteration has absorption at band 8 caused by Mg-OH, broad absorption at band 4 caused by iron in chlorite or epidote, no absorption at band 6 (Figure 2.2) and appear as pale green in the SWIR false color image. Calcite has absorption at band 8 caused by $CO_3$, but does not have absorption at band 4 because calcite lacks iron and no absorption at band 6 (Figure 2.2) and appears as yellow in the SWIR false color image.

VNIR false color and natural color images provide more detailed surface information compared to the 30 m resolution SWIR false color image and are useful as map images for field surveys. The most recent image with the least cloud coverage should be chosen for use in field surveys due to differences in the surface condition such as new roads and architectural structures. The image created from band operation (R:G:B=b2: (b1*b3+b3)/b4:b1) using only the VNIR bands also has 15 m spatial resolution and has similar colors to a true color image created by red, green and blue wavelength images (ERSDAC, 2003). The VNIR false color image created by applying ASTER RGB bands 3, 2, and 1 to R, G, B, respectively, has 15 m spatial resolution and is useful for interpreting the surface. While it is not able to identify alteration from the spectral features, it could be used to distinguish whether the alteration is caused by hydrothermal activity or weathering because of its usefulness in identifying surface textures. The appearance of alteration caused by weathering differs from hydrothermal alteration, generally appearing as a uniform alteration mineral assemblage and the shape of the alteration is usually concordant with the distribution of the geological unit. The band combinations for the false color images used in this study are summarized in Table 2.2.

2.4.3 Band ratio color composite image

Alunite and kaolinite are the main alteration minerals present in the advanced argillic alteration. Alunite and kaolinite both have absorption at ASTER bands 5 and 6 in the

SWIR region. Alunite has a deep broad absorption at band 5 that also creates absorption at band 6. Kaolinite has separate absorptions at bands 5 and 6, and band 6 has a deeper absorption compared to band 5 (Figure 2.2). Alunite and kaolinite identification can be enhanced by band ratios of b4/b5 or b4/b6 (Figures 2.4 (a), (b)).

Sericite is the main alteration mineral present in the phyllic alteration. Sericite has a single deep absorption at ASTER band 6. Sericite can be enhanced by band ratio b5/b6 (Figure 2.4 (c)).

Chlorite and epidote are the main alteration minerals present in the propylitic alteration. They have absorption at ASTER band 8. Calcite, which is a common mineral in marble and at the surface, also has absorption at band 8. Chlorite, epidote and calcite can be enhanced by band ratio b5/b8 (Figure 2.4 (d)).

Advanced argillic alteration, phyllic alteration, propylitic alteration and calcite can be identified by the color composite image of band ratios by applying advanced argillic alliteration to red, phyllic alteration to green and propylitic alteration to blue (R:G:B=4/6:5/6:5/8). The alteration assemblage can be estimated from the resultant color combination. We choose to use the band ratio b4/b6 to enhance advanced argillic alteration because it is strongly enhanced compared to phyllic and propylitic alteration as opposed to when band ratio b4/b5 is used in the band ratio color composite image.

### 2.4.4 Principal component analysis color composite image

PCA is a statistical method to reorganize data into several common factors using a linear transformation that projects data onto a new orthogonal axes coordinate. PCA is also used for separating information and noise in remote sensing data processing. The Crosta method is known for obtaining information of alteration zones using PCA to Landsat data (Crosta and Moore, 1989; Loughlin, 1991). The Crosta method has been also applied to ASTER data (Crosta et al., 2003). The main feature of the Crosta method is to use only four bands for PCA to make interpretation of the PCA images easier. In order to obtain PCA images with information about alteration, appropriate selection of the four bands for the PCA is necessary. The eigenvector values need to be checked to determine the optimal PCA image for displaying the distribution of a specific alteration.

We conducted PCA using ASTER data to identify the same alteration types as in our band ratio method. Four bands are chosen for PCA to identify advanced argillic alteration (alunite, kaolinite), phyllic alteration (sericite) and propylitic alteration (chlorite, epidote) and calcite (Table 2.3). ASTER bands 1, 4, 6, and 7 are used to generate a PCA image that features absorption at band 6 for indicating advanced argillic alteration (alunite, kaolinite). ASTER bands 1, 3, 5, and 6 are used to generate a PCA

image that features sharp absorption at band 6 for indicating phyllic alteration (sericite). ASTER bands 1, 3, 5, and 8 are used to generate a PCA image that features absorption at band 8 for indicating propylitic alteration (chlorite, epidote) and calcite.

Four PCA images are created by conducting PCA using ASTER bands 1, 4, 6, and 7 to identify advanced argillic alteration (alunite, kaolinite). The PCA image having absorption features at band 6 in the eigenvalues needs to be identified. The advanced argillic alteration image has either positive eigenvalues for bands 4 and 7 and a negative value for band 6, or conversely, negative eigenvalues for bands 4 and 7 and a positive value for band 6. To identify phyllic alteration (sericite), four PCA images are created by conducting PCA using ASTER bands 1, 3, 5, and 6. The PCA image having absorption features at band 6 in the eigenvalues needs to be identified. The PCA image that has a positive eigenvalue for band 5 and a negative value for band 6, or the converse, is the phyllic alteration image. To identify propylitic alteration (chlorite, epidote) or calcite, four PCA images are created by conducting PCA using ASTER bands 1, 3, 5, and 8. The PCA image having absorption features at band 8 in the eigenvalues needs to be identified. The PCA image that has a positive eigenvalue for band 5 and a negative value for band 8, or the converse, is the propylitic alteration (chlorite, epidote) or calcite image. Whether specific eigenvalues are positive or negative depends on the input ASTER data and when the eigenvalues have opposite features to the spectral absorption, the PCA image needs to be inverted. After each alteration image is defined, a PCA color composite alteration image applying R: G: B=advanced alteration image: phyllic alteration image: propylite alteration/calcite image can be obtained. This PCA color composite image will have similar features to the band ratio color composite image, displaying the three types of alteration in different colors.

## 2.5 Processed image results

### 2.5.1 False color images

Examples of a natural color image and SWIR false color image are shown in Figures 2.5 (a) and (b) for the case study site. The Meiduk deposit, two alteration zones to the northwest (alteration A), southeast (alteration B) and one alteration zone to the north of the Meiduk deposit (alteration C) appear as a pinkish color in the SWIR false color image. These are inferred to be hydrothermal alteration because they are not concordant with the lithological unit that hosts the alteration. On the other hand, the alteration zone to the northeast that appears as a light pinkish color (alteration D) is inferred to be alteration caused by weathering because it is concordant with the lithological unit

(probably a sedimentary unit) that hosts the alteration. Hydrothermal alteration that is accompanied by porphyry copper mineralization generally appear as bleached alteration at surface and displays a white to white yellow color in the VNIR false color image or natural color image. There are also areas that appear as pale green in the northern part of the SWIR false color image (alteration E and F), and are inferred as propylitic alteration.

2.5.2 Band ratio color composite image

An example of a band ratio color composite image is shown in Figure 2.5 (c). This image is displayed in original contrast without contrast stretching. The Meiduk deposit and the two alteration zones present on the NW-SE trending mountains located northwest (alteration A) and southeast (alteration B) of the Meiduk deposit appear as yellow to red in this image. This alteration is estimated as a combination of advanced argillic alteration and phyllic alteration from its color created as a mixture of red and green. A small zone of blue is present around the yellow to red area at the center of the image and green surrounds it across a wide area. This indicates the zonation of advanced argillic alteration and phyllic alteration at the center and propylitic alteration, and weak alteration (smectite) as surrounding alteration zones of the hydrothermal alteration. Thus, we have shown that the alteration types are displayed in different colors in the band ratio color composite image.

Alteration C that is located to the north appears as mainly red in color and indicates alunite or kaolinite alteration. Alteration D that appeared as light pink in the SWIR false color image appear as light yellow to light blue in color in the band ratio color composite image and is inferred as weathering alteration (kaolinite, smectite) in a calcareous sedimentary unit by the shape of the alteration. The alteration zones E and F that are located to the north appear as pale green in the SWIR false color image and blue in the band ratio color composite image are estimated as chlorite, epidote alteration. Area G appears widely as a green color in the band ratio color composite image and inferred to be a weakly weathered alteration consisting of smectite.

2.5.3 Principal component analysis color composite image

An example PCA color composite image for the case study site is shown in Figure 2.5 (d). This image is also displayed in original contrast without contrast stretching. This color composite image is created from the advanced argillic alteration image, phyllic alteration image and propylitic alteration image obtained from PCA, respectively.

While the green color appears weaker, the color information obtained from the PCA color composite image is very similar to the band ratio color composite image.

## 2.6 Discussion

### 2.6.1 False color images

Different variations of SWIR false color images were investigated and applying bands 4, 6 and 8 to red, green, blue, respectively, produced the best false color combination for the exploration of porphyry copper deposits and geological mapping because absorption of important minerals occur at bands 6 and 8. Band 4 is used as a stable input in the SWIR false color image because most minerals do not have absorption at band 4 and it generally has high reflectance. The possibility of introducing the higher resolution VNIR image into the false color combination has been examined, and was not found to add value since band 6 and band 8 could not be exchanged in order to identify the absorption features of the alteration minerals. Additionally, as the reflectance of bands 1, 2 and 3 do not have higher reflectance than band 4, the absorption features at band 6 and band 8 could not be enhanced. Adjustment of the spatial resolution is also required to create a false color image combining the VNIR and SWIR bands. Therefore, we conclude that the SWIR false color image applying bands 4, 6, and 8 to red, green, blue, respectively, is the optimal image for identification of alteration. This false color image is fast and easy to create since it uses only the bands in the SWIR. In the SWIR false color image, advanced argillic alteration and phyllic alteration appear as pink, propylitic alteration appears as green and calcareous units appear as yellow as distinct features identifiable without error.

The pink color in the SWIR image may not always be hydrothermal alteration as it could be alteration created by weathering. Kaolinite is a common alteration mineral produced from weathering, aericite is produced from weathering of sedimentary units and gypsum is produced from evaporates. Weathering alteration appears as concordant with the geological unit and generally do not have a zonation of alteration. Weathering alteration can be distinguished by comparing the shape of alteration and the geological unit in the VNIR false color image or natural color image. In an ideal situation, the primary hydrothermal alteration appears as a circular to ovoid shape, but the shape is often controlled by fractures and faults and appear in various forms. The size of hydrothermal alteration is generally smaller depending on the scale of hydrothermal activity. Cross checking using the VNIR false color image or the natural color image having higher resolution than the SWIR false color image is recommended for accurate identification of hydrothermal alteration for exploration.

2.6.2 Band ratio color composite image

Advanced argillic alteration tends to appear more clearly than phyllic and propylitic alteration in remote sensing images because alunite and kaolinite have stronger spectral absorption features compared to sericite, smectite, chlorite, epidote and calcite in the SWIR wavelength region. This is confirmed by comparing the band ratio images of Landsat and ASTER. The band ratio band 5/band 7 is used to identify alteration zones for Landsat (Figure 2.6 (a)). The band ratio image of Landsat band 5/band 7 is similar to the band ratio images of ASTER band 4/band 5 and band 4/band 6 (Figures 2.4 (a), (b)), which indicates that advanced argillic alteration is mainly identified in the band ratio image of Landsat (band 5/band 7). For the same reason, we choose to use the band ratio of band 4/band 6 to enhance advanced argillic alteration in the ASTER band ratio color composite image (R:G:B=4/6:5/6:5/8) instead of (R:G:B=4/5:5/6:5/8) because the advanced argillic alteration appear in excess when using the band ratio band 4/band 5 in the band ratio color composite image compared to phyllic and propylitic alteration.

Phyllic alteration is enhanced when using the band ratio image of ASTER (band 5/band 6), but the known porphyry copper mineralization related phyllic alteration zones display yellow to yellow green colors in the ASTER band ratio color composite image. The yellow to yellow green colors are obtained from mixing of alteration zones obtained from band ratios band 4/band 6 and band 5/band 6. The band ratio for enhancement of sericite is ASTER band 5/band 6, but green in the band ratio color composite image does not match with the distribution of sericite alteration. Sericite can be also enhanced by band ratio band 4/band 6 with regard to the spectral pattern (Figure 2.2) and could appear in yellow to yellow green colors without mixture of advanced argillic alteration. Phyllic alteration is also identified in the ASTER band ratio color composite image (R:G:B=4/5:5/6:5/8), which enhances the advanced argillic alteration more efficiently. Band ratio for enhancement of kaolinite is ASTER band 4/band 6, but kaolinite is also enhanced by band ratio band 5/band 6 without mixture of phyllic alteration. It is difficult to identify whether the alteration consists of kaolinite or sericite only from the ASTER band ratio color composite image. In order to identify kaolinite and sericite accurately, interpretation of ASTER spectral data using atmosphere corrected reflectance data is necessary (Figure 2.2 right). Alunite in advanced argillic alteration always appears in red in the ASTER band ratio color composite image. The green color present surrounding the hydrothermal alteration is weak alteration of smectite that is created by weathering.

Propylitic alteration (chlorite, epidote) and calcareous units and alteration (calcite) are enhanced when using the band ratio image of ASTER band 5/band 8, but absorption caused by Mg-OH at band 8 is weak and unclear compared to the absorption of Al-OH at band 6. This occurs because rocks with propylitic alteration are green in color, which has lower reflectance. As a result, propylitic alteration is not identified as clearly as the bleached alteration of advanced argillic and phyllic alteration in the ASTER band ratio color composite image. Propylitic alteration is a periphery alteration zone of porphyry copper mineralization and the amount of alteration minerals is not abundant. The limited distribution of the blue color accompanying the advanced argillic and phyllic alteration is appropriate. Cross checking the green color in the ASTER SWIR false color image is necessary in order to identify propylitic alteration accurately.

### 2.6.3 Principal component analysis color composite image

The PCA color composite image can be used to obtain information on alteration similar to the ASTER band ratio color composite image and provides an additional method to obtain information on alteration and alteration minerals. While PCA requires more data processing steps, the identification results are in most cases more appropriate using PCA of four bands than the results obtained from a band ratio using only two bands. This is particularly the case for vegetated terrain because alteration and vegetation have similar spectral patterns in the SWIR region that cannot be distinguished by using two bands for the band ratio.

It has been found that PCA color composite images created from Landsat data are able to identify alteration zones more clearly compared to false color images (Loughlin, 1991; Tangestani and Moore, 2002). A Landsat PCA color composite image uses a combination of iron oxide and alteration images (R:G:B= alteration image: alteration + iron oxide image: iron oxide image). Alteration zones are identified clearly and appear as yellow in the Landsat PCA color composite image (Figure 2.6 (b)), but there are some weaknesses compared to the ASTER PCA color composite image: 1) atmospheric correction of Landsat data is necessary in order to obtain accurate iron oxide distribution; 2) alteration identified from Landsat data is mainly advanced argillic alteration; and 3) alteration is identified without providing information on the alteration zones. Therefore, the ASTER PCA color composite image is more practicable than the Landsat PCA color composite image because it is able to provide information on three alteration types (advanced argillic, phyllic and propylitic alteration) using five bands in the SWIR region (2.0 to 2.5 μm) without atmospheric correction.

2.6.4 Effect of the atmosphere

Satellite images are affected by the atmosphere between the sensor and surface topography (Iikura and Yokoyama, 1999). The atmosphere causes scattering effects in the visible wavelength region, but not in the infrared region. Spectral features at wavelength regions that are not largely affected by the scattering and absorption effects of the atmosphere maintain the spectral features in plesiomorphism (Ono et al., 2002). We compared ASTER level 1 data, which is radiance data, and ASTER level 2 data, which is atmosphere corrected surface reflectance data. ASTER band 1 and band 2 of level 1 data are affected by scattering compared to ASTER level 2 data (Figure 2.7). Bands 7 and 9 have different features between ASTER level 1 and level 2 data, but this difference is small and does not affect the results of band ratios band 4/band 6, band 5/band 6 and band 5/band 8 used in this study. We created a band ratio color composite image and a PCA color composite image using atmosphere corrected ASTER level 2 surface reflectance data (Figures 2.8 (a), (b)) to compare with the images obtained using ASTER level 1 radiance data (Figures 2.5 (c), (d)). There is not a large difference between the band ratio and PCA color composite images created using ASTER level 1 and level 2 data. This result confirms that adequate band ratio and PCA color composite images are obtained using ASTER level 1 data, but atmosphere corrected ASTER data is necessary for accurate mineral identification using spectral information. It is recommended that band ratio and PCA color composite images are created using atmosphere corrected ASTER data for detailed interpretation of the image and spectral information. We interpreted the spectral information of the alteration zones using ASTER level 2 data (Figure 2.8 A to G). It has been clarified that the alteration zones consist of alunite, kaolinite, sericite, chlorite, etc., and that the band ratio and PCA color composite images are indicating advanced argillic, phyllic and propylitic alterations correctly.

Vegetation has two clear spectral features in the VNIR region, being: 1) green in color, and 2) highly reflective in the near infrared region. The quality of atmospheric correction can be evaluated by checking the spectral pattern of vegetation in the ASTER image. The spectral pattern of vegetation from ASTER level 2 data is shown in Figure 2.8 H. The green color of vegetation is indicated by higher reflectance of band 1 compared to band 2, which are the green and red bands, respectively. The most characteristic feature of vegetation appear as extremely high reflectance at band 3 and low reflectance at band 2, which are the near infrared and red bands, respectively. Hence, ASTER level 2 data provide correct spectral information for the scene used in this study determined from the spectral features of vegetation.

We do not introduce the iron oxide image created from ASTER bands 1 and 2 because these bands are strongly affected by the scattering effect of the atmosphere. Correct iron oxide distribution cannot be obtained using ASTER level 1 data and atmospheric correction of band 1 is difficult depending on the condition of the atmosphere.

## 2.7 Conclusions

ASTER data processing methods for exploration of porphyry copper deposits have been studied and we have clarified that false color images, band ratio and PCA color composite images made from ASTER data provide accurate information on alteration and geology. The ASTER images are created from simple procedures and are always reproducible. They provide more information of alteration zoning and minerals than Landsat data.

The ASTER SWIR false color image (R:G:B=4:6:8) displays advanced argillic and phyllic alterations in a pinkish color, propylitic alteration in a greenish color and calcareous units in yellow and are easily identified from the image. The ASTER band ratio color composite image (R:G:B=4/6:5/6:5/8) and ASTER PCA color composite image (R:G:B=PCA advanced argillic alteration image: PCA phyllic alteration image: PCA propylitic alteration image) are able to discriminate between advanced argillic, phyllic and propylitic alterations and combinations by color. PCA uses four ASTER bands to obtain the PCA alteration band, and is able to identify alteration precisely over difficult terrains such as areas with vegetation compared to the band ratio image. The ASTER false color images, band ratio and PCA color composite images provide correct results using ASTER level 1 data that are not atmospherically corrected, but in order to conduct accurate mineral identification between kaolinite and sericite, the images should be created using atmospherically corrected data that have correct spectral information.

Hydrothermal and weathering alteration can be discriminated by the mode of occurrence. Hydrothermal activity creates zoning of advanced argillic, phyllic and propylitic alterations due to the difference in temperature of the hydrothermal fluid. Weathering alteration generally does not have alteration zonation and appear concordantly with the lithological unit.

In conclusion, we have shown that identification of hydrothermal alteration zones over wide areas is possible and detailed information on alteration for the purposes of exploration of porphyry copper deposits can be obtained using the proposed ASTER image creation methods.

Table 2.1 ASTER, Landsat7ETM+ band specifications.

| Sensor | ASTER | | | | Landsat7ETM+ | | | |
|---|---|---|---|---|---|---|---|---|
| | Band number | Spectral range (μm) | Central wave length (μm) | Spatial resolution (m) | Band number | Spectral range (μm) | Central wave length (μm) | Spatial resolution (m) |
| VNIR | | | | | band1 | 0.452-0.514 | 0.485 | 30 |
| | band1 | 0.52-0.60 | 0.556 | 15 | band2 | 0.519-0.601 | 0.575 | 30 |
| | band2 | 0.63-0.69 | 0.661 | 15 | band3 | 0.631-0.692 | 0.660 | 30 |
| | band3N | 0.78-0.86 | 0.807 | 15 | band4 | 0.772-0.898 | 0.830 | 30 |
| | band3B | 0.78-0.86 | 0.804 | 15 | band8 | 0.515-0.896 | 0.705 | 15 |
| SWIR | band4 | 1.60-1.70 | 1.656 | 30 | band5 | 1.547-1.748 | 1.663 | 30 |
| | band5 | 2.145-2.185 | 2.167 | 30 | band7 | 2.065-2.346 | 2.193 | 30 |
| | band6 | 2.185-2.225 | 2.208 | 30 | | | | |
| | band7 | 2.235-2.285 | 2.266 | 30 | | | | |
| | band8 | 2.295-2.365 | 2.336 | 30 | | | | |
| | band9 | 2.360-2.430 | 2.400 | 30 | | | | |
| TIR | band10 | 8.125-8.475 | 8.291 | 90 | band6 | 10.31-12.36 | | 60 |
| | band11 | 8.475-8.825 | 8.634 | 90 | | | | |
| | band12 | 8.925-9.275 | 9.075 | 90 | | | | |
| | band13 | 10.25-10.95 | 10.657 | 90 | | | | |
| | band14 | 10.95-11.65 | 11.318 | 90 | | | | |

Table 2.2 ASTER bands used for false color images.

| Color | Alteration image | VNIR image | Natural color image (ERSDAC, 2003) |
|---|---|---|---|
| Red (R) | band4 | band3 | band2 |
| Green (G) | band6 | band2 | (band1×3+band3)/4 |
| Blue (B) | band8 | band1 | band1 |

Table 2.3 ASTER bands used for band ratio image and PCA image.

| Color | Alteration | Band ratio | PCA |
|---|---|---|---|
| R | Advanced argillic | band4/band6 | band1, 4, 6, 7 |
| G | Phyllic | band5/band6 | band1, 3, 5, 6 |
| B | Propylitic | band5/band8 | band1, 3, 5, 8 |

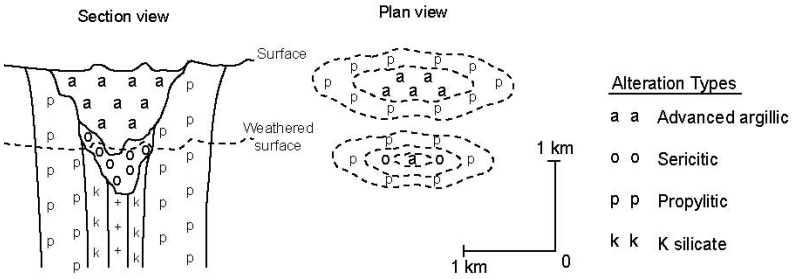


Figure 2.1 Typical alteration zoning related to porphyry copper mineralization (modified after Sillitoe, 2000).

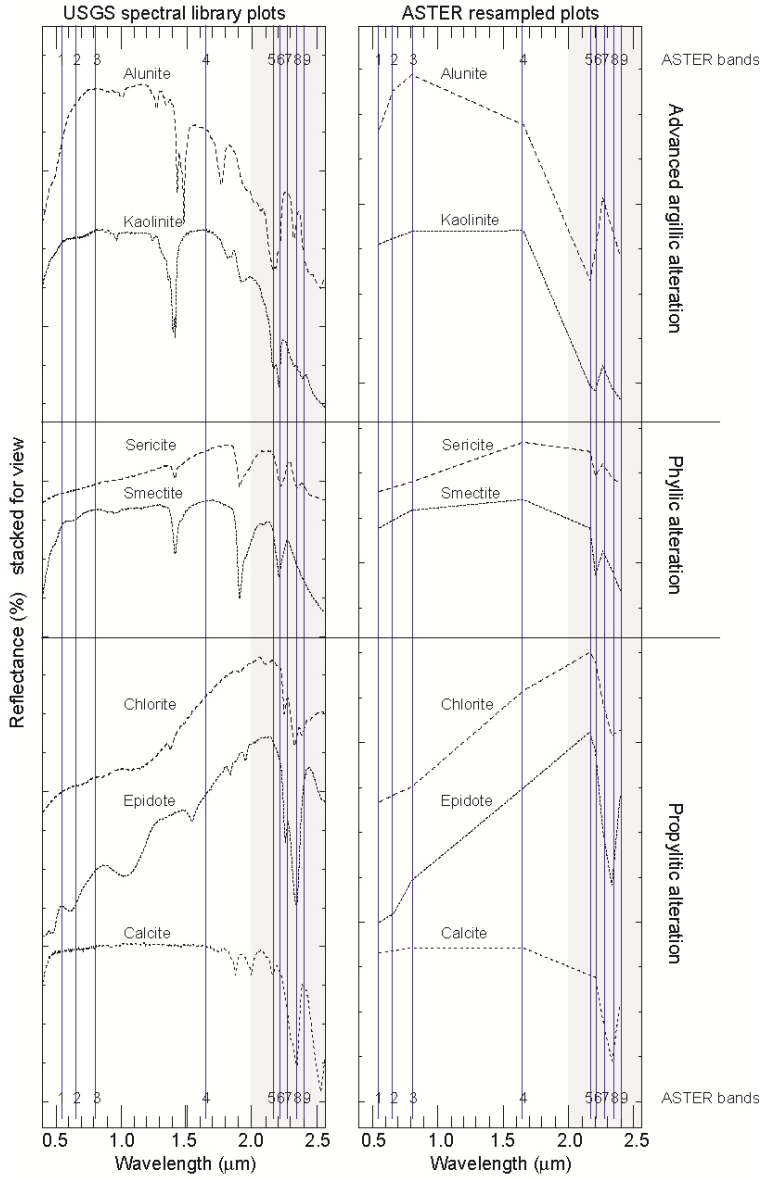


Figure 2.2 Spectral reflectance and ASTER simulated spectral patterns of alteration minerals related to porphyry copper mineralization.

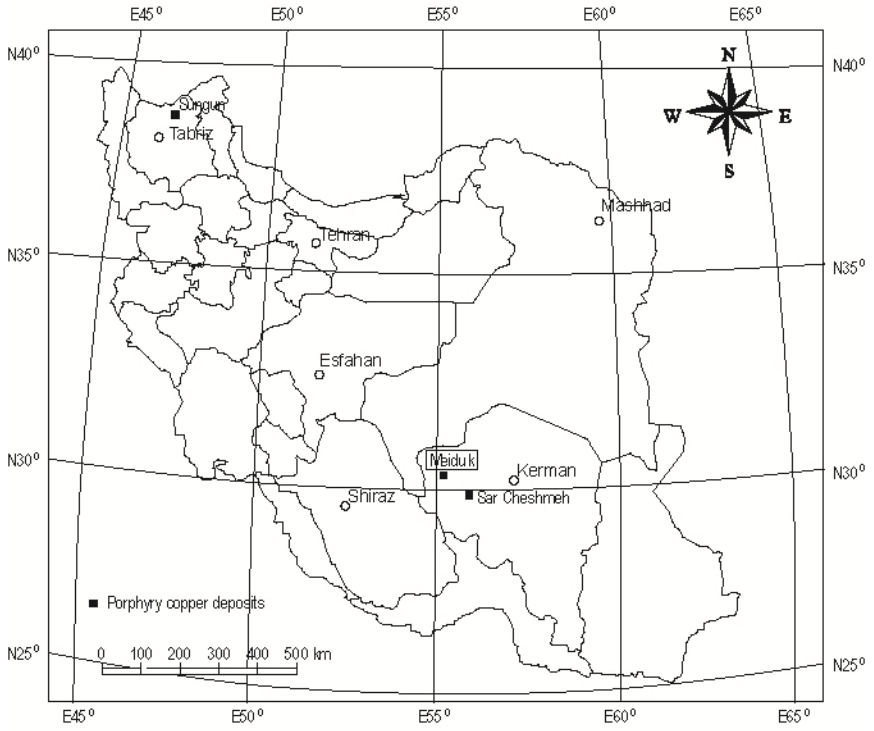


Figure 2.3 The study area (Meiduk) for the ASTER data processing.

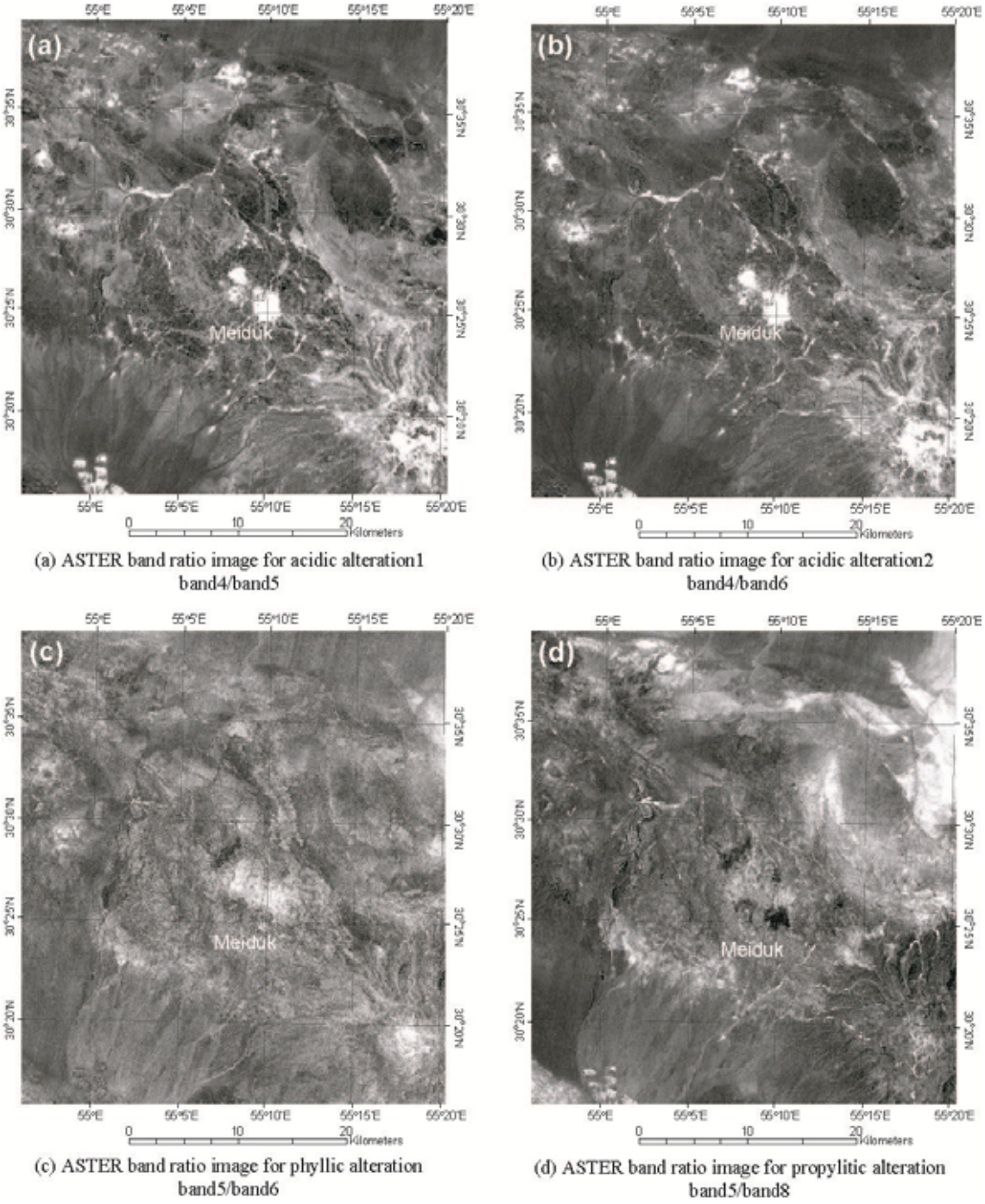


(a) ASTER band ratio image for acidic alteration1 band4/band5

(b) ASTER band ratio image for acidic alteration2 band4/band6

(c) ASTER band ratio image for phyllic alteration band5/band6

(d) ASTER band ratio image for propylitic alteration band5/band8

Figure 2.4 ASTER band ratio images for detection of alteration zones.

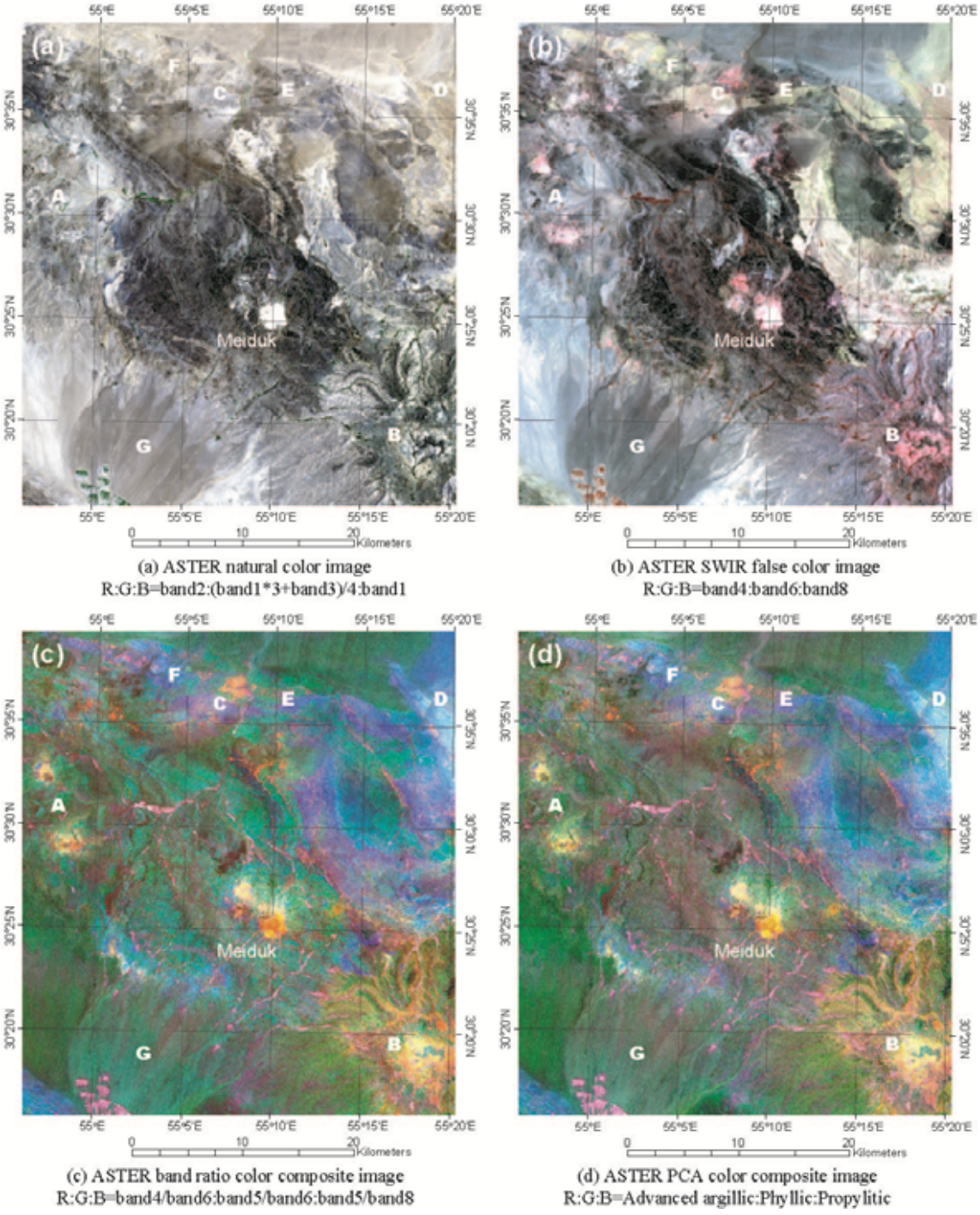


(a) ASTER natural color image
R:G:B=band2:(band1*3+band3)/4:band1

(b) ASTER SWIR false color image
R:G:B=band4:band6:band8

(c) ASTER band ratio color composite image
R:G:B=band4/band6:band5/band6:band5/band8

(d) ASTER PCA color composite image
R:G:B=Advanced argillic:Phyllic:Propylitic

Figure 2.5 ASTER false color and color composite images for detection of alteration zones.

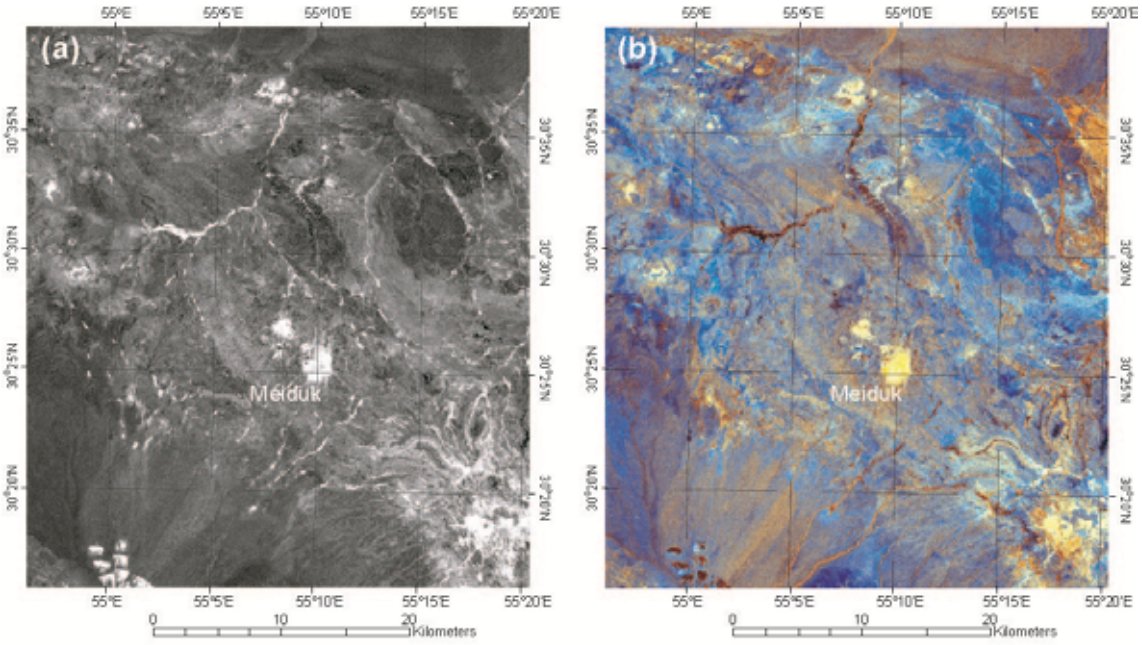


(a) Landsat7 band ratio image for hydroxyl (alteration) band5/band7

(b) Landsat7 PCA image for detection of alteration zones. R:G:B=Hydroxyl:Hydroxyl+Iron-oxide:Iron-oxide

Figure 2.6 Landsat7 band ratio image and PCA color composite image for detection of alteration zones.

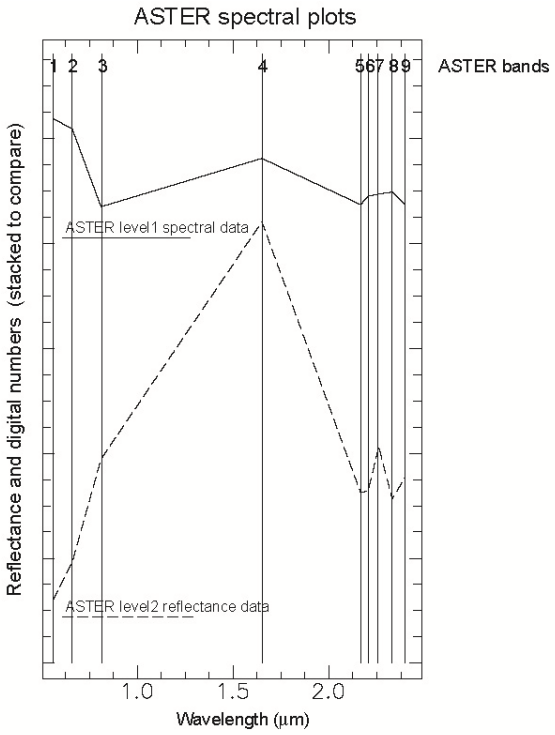


Figure 2.7 Spectral patterns of alunite derived from ASTER level1 and level2 data.

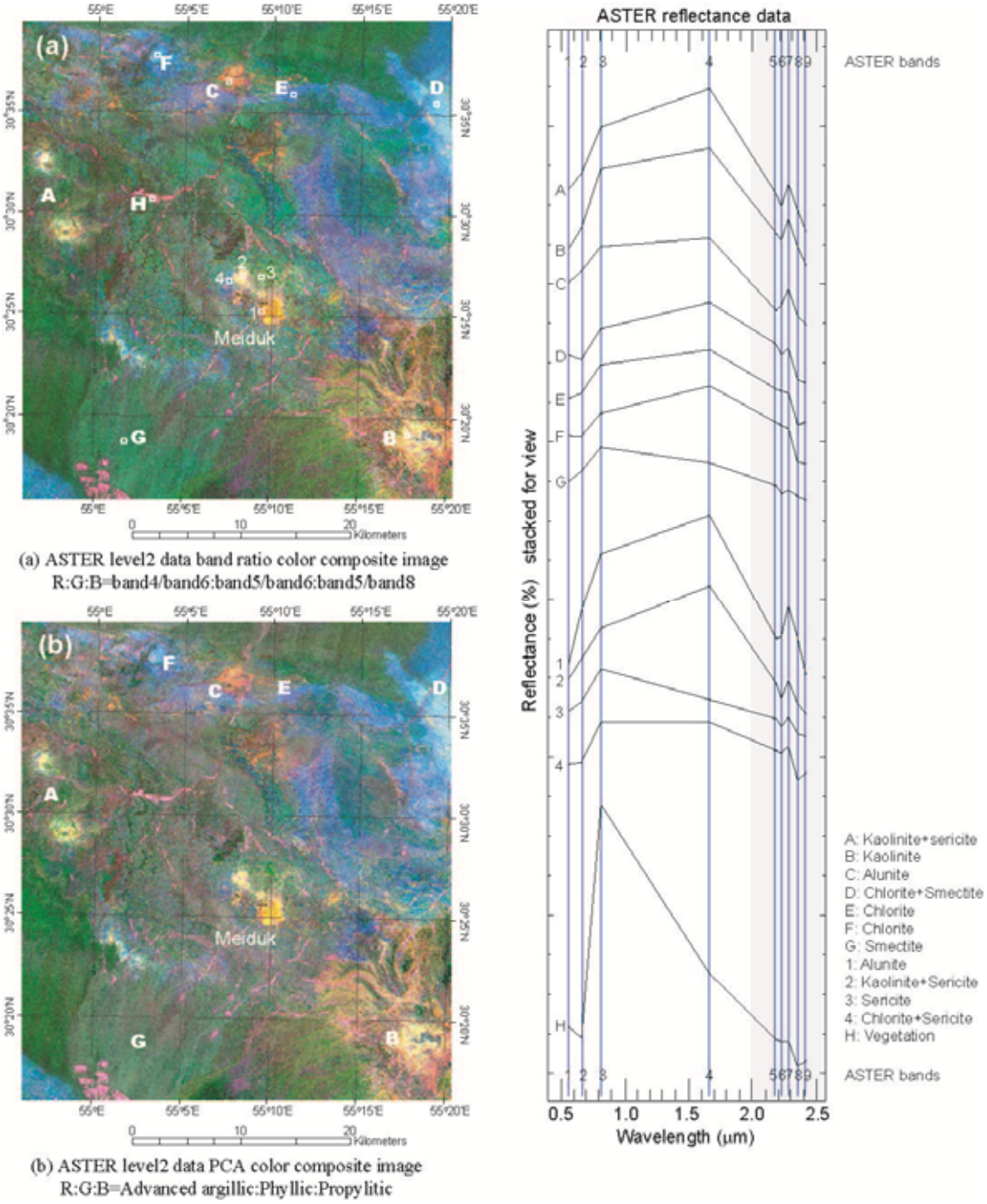


Figure 2.8 ASTER level2 data color images for detection of alteration zones and ASTER representative surface reflectance data.

# CHAPTER 3

## Geological mapping of the Francistown area in northeastern Botswana by surface temperature and spectral emissivity information derived from Advanced Spaceborne Thermal Emission and Reflection Radiometer (ASTER) thermal infrared data

### 3.1 Introduction

Remote sensing can provide valuable information about the earth surface and is useful for geological mapping and mineral exploration (Lyon and Lee, 1970; Goetz and Rowan, 1981). Spectral information in the visible and near-infrared (VNIR) region is useful for identifying iron-bearing minerals such as goethite and hematite (Fraser, 1991) and for assessing vegetation. Spectral absorption features due to the vibrations of Al–OH, Mg–OH, and $CO_3^{2-}$ bonds in the shortwave infrared (SWIR) region are useful for identifying hydrothermal alteration and carbonate minerals (Hunt, 1977). Mineral mapping based on VNIR and SWIR data can be used to identify mineralization that is accompanied by hydrothermal alteration or magmatic intrusions related to greisen and hornfels alteration. However, magmatic ore deposits such as Ni-PGE sulfide deposits are not usually accompanied by extensive alteration. To identify magmatic ore deposits that are not accompanied by significant alteration, it is important to develop a method for identifying geological units that host or accompany mineralization (such as mafic-to-ultramafic and granitic units) from remote sensing data.

Spectral emissivity features due to the lattice vibration of Si–O in the thermal infrared (TIR) region are useful for identifying silicate rocks and minerals. Early geological studies employing TIR data used a single TIR band. A difference in thermal properties has been used to identify geological units (Lyon, 1972; Watson, 1975; Kahle and Rowan, 1980; Abrams et al., 1984) and the thermal inertia method has been used to distinguish different rock types (Kahle, 1976; Price, 1977; Kahle et al., 1984). For example, basalt, gabbro, alluvium, moist areas, and vegetation have been discriminated from thermal inertia images. However, thermal inertia imaging requires obtaining day and night images of the same area with a small time difference, which restricts its usefulness.

After the development of multiband TIR sensors such as the airborne TIMS (Kahle and Goetz, 1983) and MASTER (Hook et al., 2001) and subsequently the spaceborne ASTER (Yamaguchi et al., 1998), spectral emissivity information of TIR data has been actively used for geological applications (Gillespie et al., 1984; Sabine et al., 1994; Rockwell and Hofstra, 2008; Taranik et al., 2009). Quartz, carbonate, and mafic indices

have been proposed to enhance the spectral features of ASTER TIR data (Ninomiya et al., 2005; Ninomiya and Fu, 2010). However, the quartz, carbonate, and mafic index images were often noisy. Moreover, we found that these indices do not always provide accurate distributions of carbonate and mafic units. In this paper, we propose a simple and effective method for generating false color composite (FCC) images from TIR data that allows us to identify rock units based on surface temperature and spectral emissivity information. In particular, this method can be used to map mafic-to-ultramafic units (40–45 % $SiO_2$) and felsic units such as granite (60–80 % $SiO_2$), which are important targets for mineral exploration.

3.2 Data used in this study

There are few spaceborne remote sensing systems equipped with TIR band sensors that acquire data with sufficiently high spatial resolutions for geological identification; they include ASTER and Landsat. This study uses ASTER TIR data with five spectral bands and a spatial resolution of 90 m.

VNIR and SWIR sensors measure solar energy reflected from the Earth's surface in the 0.4–2.4 μm range, whereas the TIR sensor measures outgoing thermal IR energy emitted from the Earth's surface in the 8.0–12.0 μm range. Consequently, useful TIR data can be acquired during the day and night. We used ASTER L1B day time to create FCC images for identifying geological units. FCC images are also generated from night time data to clarify the suitability of the proposed method for geological mapping.

TIR radiation is expressed as a function of temperature and emissivity. We used ASTER L2 day time data products of surface kinetic temperature (2B03) and emissivity (2B04), which were derived from the TIR radiance data by the temperature/emissivity separation algorithm (Gillespie et al., 1998). Table 3.1 lists the ASTER data used in this study.

The appearance of VNIR, SWIR, and TIR data obtained from the same location varies with acquisition date. Surface objects are sensitive to climatic conditions such as rainfall, soil moisture, solar elevation, and surface temperature. The presence of dry and senesced vegetation with lignin and cellulose absorptions can severely affect mineral mapping with SWIR data (Rockwell, 2009; John et al., 2010). VNIR data display significant seasonal variation related to changes in the occurrence patterns of green vegetation. Vegetation also affects the appearance of day time and night time ASTER TIR images, which hinders geological interpretation. September to October is the best time of the year to obtain TIR images for geological interpretation in Botswana because it is the end of the dry season when there is less green vegetation than at other times of

year and the solar elevation is high.

Another problem that affects TIR data is fire activity. Man-made fires are commonly used in the African savanna to clear surface vegetation for farming and pasture grazing. Burned areas remain hot for several weeks after a fire has been extinguished. These hot areas appear as saturated regions in TIR images and exhibit abnormal color balance and contrast. The MODIS burned area products (Roy, 2005) that visualize the distribution of burned areas are helpful for selecting an appropriate ASTER scene for geological mapping from TIR data.

### 3.3 Geology and ore deposits of Francistown area

The study area is located in the northeastern region of Botswana and includes Francistown, the second largest city in the country (Figure 3.1). Most of the land in Botswana is covered by Cenozoic Kalahari sand; in southwestern Botswana, there is unconsolidated sand whose thickness exceeds 200 m (Smith, 1984). Outcropping basement areas are limited to the eastern and southeastern parts of the country and are included in the study area. The climate of the study area is dry savanna, which is suitable for geological mapping and interpretation by remote sensing due to sparse vegetation and good outcrop conditions.

Francistown is a mining district where nickel, copper, and gold are mined. The study area is located at the southwestern edge of the Zimbabwe craton (Figure 3.1), which was developed between ~2710 and ~2647 Ma and contains many greenstone units including granite and mafic-to-ultramafic units (McCourt et al., 2004). The country rocks of the study area include Archean gneiss, schist, and metasedimentary units. The Tati and Vumba greenstone belts contain amphibolite, gabbro (mafic), serpentinite (ultramafic), and intercalated sediments (Maier et al., 2008; Fiorentini et al., 2012). The Tati greenstone belt, dated ca. 2.7 Ga (Van Geffen, 2004), and the Vumba greenstone, dated ca. 2.7 Ga (Bagai et al., 2002) are contemporaneous with the ca. 2.7 Ga Upper Bulawayan greenstones in Zimbabwe (Carney et al., 1994). Both the country rocks and greenstone units are cut by Paleozoic mafic sills of dolerite composition. Figure 3.2 (a) indicates the general geology of the study area.

The Tati greenstone unit contains operating mines, including the Tati mine (magmatic Ni–Cu–(PGE) sulfide) and the Mupane mine (orogenic Au). Moreover, the greenstone units contain many mineral occurrences (including Selkirk (magmatic Ni sulfide) and Somerset (orogenic Au)) (Baldock et al., 1976). Most of the ore deposits in the area are related to mafic-to-ultramafic and granitic magmatism. Mafic-to-ultramafic units are common host rocks for magmatic platinum, chromium, and nickel deposits and are

important targets for mineral exploration of magmatic ore deposits (Naldrett, 2010; Naldrett, 2004). Felsic granitic units accompany Archean orogenic Au and Cu mineralization, making them important targets (Partington and Williams, 2000).

## 3.4 TIR images for geological interpretation

### 3.4.1 ASTER L1B day time TIR FCC image

To generate an ASTER L1B day time TIR FCC image for geological mapping and interpretation, we respectively assigned red, green, and blue (R:G:B) to band 14:band 12:band 10. This FCC image uses the ASTER TIR bands with the shortest and longest center wavelengths. These bands were selected because adjacent ASTER TIR bands are highly correlated with each other, which results in less color contrast in the FCC image. Figure 3.2 (b) indicates an ASTER L1B day time TIR FCC image of the study area. It essentially contains six colors. Comparison with a geological map indicates that the light red regions match granitic units. The white regions match well with the greenstone units that consist of mafic-to-ultramafic units and also dolerite sills. Light green regions match the gneiss country rocks, whereas dark regions match lakes and water drainage areas.

Caution is needed for geological interpretation using the L1B day time TIR FCC image. Some granites with protruding topographic features have much denser vegetation and are indicated by light blue. The dark red regions do not indicate the distribution of quartz rich felsic units; rather, they indicate agricultural or grazing areas where vegetation has been removed.

### 3.4.2 ASTER L2 day time TIR temperature image

We used ASTER L2 day time TIR surface kinetic temperature data to compare the surface temperatures of different geological units in the ASTER L1B day time TIR FCC image. Mafic-to-ultramafic units such as the Tati and Vumba greenstone and dolerite sills appear white in the ASTER L2 day time TIR temperature image (Figure 3.2 (c)). The mafic-to-ultramafic units have higher surface temperatures than the other geological units. Felsic units appear dark in color. The darkest color matches with lakes and water drainage areas. Most drainage systems in the study area are dry and filled with river sand, but they have low temperatures due to underflow water beneath the river sand throughout the year. Local inhabitants access this underflow water by digging wells near drainage systems.

### 3.4.3 ASTER L2 day time TIR FCC image

We assigned R:G:B to band 14:band 12:band 10 to generate an ASTER TIR FCC image for geological mapping and interpretation from ASTER L2 day time emissivity data. Figure 3.2 (d) indicates ASTER L2 day time TIR FCC image of the study area. The L2 emissivity FCC image is sometimes noisy and displays less color difference than the L1B TIR FCC image (Figure 3.2 (b)) because of its narrower dynamic range

### 3.4.4 ASTER L2 broadband albedo image

To clarify the relation between the color of geological units and the temperature, a broadband albedo image was generated from the VNIR and SWIR bands of ASTER L2 reflectance data using the following formula (Liang, 2000):

Broadband albedo = 0.484*band 1 + 0.335*band 3 – 0.324*band 5 + 0.551*band 6 + 0.305*band 8 – 0.367*band 9 – 0.0015

The bright areas match the high-albedo quartz-rich felsic units and the dark areas match the low-albedo mafic-to-ultramafic units in the ASTER albedo image (Figure 3.2 (e)). Lakes and drainage with water appear as low-albedo regions, whereas dry drainage areas filled with river sand appear as high-albedo regions. The country rock gneiss appears as a moderate-albedo region. Agricultural or grazing areas appear as high-albedo regions, whereas vegetation reduces the albedo.

### 3.4.5 ASTER L2 NDVI image

To clarify the effect of vegetation on the TIR images, NDVI images are generated from the VNIR bands of ASTER L2 reflectance data. The bright (white) regions with high NDVI values indicate vegetation (Figure 3.2 (f)). The NDVI image indicates that most of the study area has sparse vegetation. Dense vegetation exists along the drainage systems or in areas with relatively high elevations. Low-albedo regions appear white in the NDVI image.

### 3.4.6 ASTER L2 day time TIR QI–CI–MI color composite image

We used the quartz index (QI), the carbonate index (CI), and the mafic index (MI) proposed by Ninomiya et al. (2005) and Ninomiya and Fu (2010) and created a color composite image by assigning R:G:B to QI:CI:MI, respectively (Figure 3.3 (a)). The QI, CI, and MI are calculated using the following formulas.

QI = (band 11*band 11)/(band 10*band 12)

CI = band 13/band 14

MI = (band 12*band $14^3$)/band $13^4$

We used ASTER L2 day time emissivity data to generate QI, CI, and MI images because the above formulas are mainly based on the spectral emissivity features of quartz, carbonate, and mafic rocks for identification. Quartz-rich units have been mapped using ASTER L2 day time emissivity data and quartz-rich rocks were highly delineated using band ratios (Hewson et al., 2005). In addition, carbonate units are well delineated using band ratios obtained from ASTER L2 day time emissivity data (Rockwell and Hofstra, 2008). We compared the day time TIR QI–CI–MI color composite image (R:G:B to QI:CI:MI) with the ASTER L1B day time TIR FCC image and interpreted these images based on spectral features in the TIR region.

There are four main colors in the ASTER L2 day time QI–CI–MI color composite image of the study area (Figure 3.3 (a)). Quartz-rich units appear in red/orange regions. Their distribution matches those of the light red regions in the ASTER L1B day time TIR FCC image and the high-albedo regions in the broadband albedo image, which indicate granitic units. Blue is thought to indicate mafic units and is expected to match the mafic-to-ultramafic units in the published geological map and the distribution of white regions in the ASTER L1B day time TIR FCC image. However, blue is distributed more widely in areas near drainage systems. Green is considered to indicate carbonate units, but the study area does not contain many carbonate units such as limestone or marble. Actually, green matches gneiss country rock in the study area. In addition, cyan indicates high CI and MI values and should thus correspond to a mixture of carbonate and mafic units; it also matches gneiss country rock across the study area. Figures 3.3 (b)–(d) respectively shows grayscale QI, CI, and MI images. The QI and CI images are noisier than the MI image, which makes the QI–CI–MI color composite image noisy.

### 3.4.7 ASTER L1B night time TIR FCC image

The ASTER L1B night time TIR FCC image (R:G:B=band 14:band 12:band 10) displays different information from the ASTER L1B day time TIR FCC image (Figures 3.4 (a) and (b)). Dolerite sills that appear as white streaks in the ASTER L1B day time TIR FCC image do not appear in the night time TIR FCC image. Dolerite sills that are not mapped on the published geological map also appear on the ASTER L1B day time TIR FCC image (Figure 3.4 (b)). White regions in the ASTER L1B night time TIR FCC

image match the distribution of vegetation, judging from the NDVI image generated from VNIR bands of ASTER L2 reflectance data (Figure 3.4 (c)). There is still a high vegetation density in May when the night time image was obtained of the study area. Vegetation is enhanced in the night time image because vegetation has a relatively high water content and has a small temperature change at night as surface vegetation cools slower than rock units at night (Price, 1977).

Because the archived ASTER night time TIR data have a limited distribution, we were unable to obtain images from a season with low vegetation cover, which are more suitable for geological mapping. It was thus difficult to extract geological information from the ASTER L1B night time TIR FCC image.

## 3.5 Discussion

### 3.5.1 Temperature information in day time TIR data

Mafic-to-ultramafic units and dolerite sills appear white in the ASTER L1B day time TIR FCC image (Figure 3.2 (b)). This indicates that these rock types have high digital values in bands 10, 12, and 14 of the ASTER L1B data. Figure 3.5 indicates the spectral emissivity patterns (8.0–14.0 μm) of typical rock samples in the study area. A Designs and Prototypes Micro FT-IR spectrometer (Model 101) was used for spectral measurements. Rock chip samples were used directly without preparation (METI/MMAJ, 2001). Mafic-to-ultramafic rocks such as gabbro and dunite exhibit similar spectral patterns. Gabbro and dunite have low emissivities in bands 13 and 14 (Figures 3.5 (a) and (b)). They are thus expected to appear as cyan in the spectral pattern, but they actually appear white in the ASTER L1B day time TIR FCC image. This suggests that temperature information dominates over spectral emissivity information in band 14.

We generated a scatter plot using the digital values of the day time TIR bands of ASTER L1B data and ASTER L2 temperature data to clarify the information contained in the ASTER L1B day time TIR data (Figure 3.6 (a)). Another scatter plot using digital values of the TIR bands of ASTER L2 emissivity data and ASTER L2 temperature data was generated (Figure 3.6 (b)). These plots exhibit the following four characteristics.

The first characteristic is that ASTER L1B bands 13 (0.9213) and 14 (0.93237) have high correlation coefficients with the L2 temperature data. This indicates that the digital values of L1B bands 13 and 14 are highly correlated with the surface temperature and that the surface temperature dominates the spectral emissivity information, as expected. The second characteristic is the low correlation coefficients with temperature for bands 10 (0.54688), 11 (0.55873), and 12 (0.44682). This indicates that bands 10, 11, and 12

provide more spectral information than bands 13 and 14. The third characteristic is that L2 emissivities have no correlation with the temperature and that most of the temperature information is removed by the emissivity conversion (Gillespie et al., 1998). The fourth characteristic is that L2 emissivities in bands 13 and 14 have smaller dispersions than those in bands 10 to 12.

We thus conclude that bands 10, 11, and 12 in the ASTER L1B day time TIR data contain both spectral emissivity and temperature information, whereas information about the surface temperature dominates over the spectral emissivity information in bands 13 and 14.

3.5.2 Relation between temperature and albedo, vegetation, and water

Another scatter plot was generated between the broadband albedos derived from the ASTER L2 VNIR-SWIR reflectance data and the ASTER L2 temperature data (Figure 3.7). The data distribution in this plot exhibits the following three characteristics.

The first characteristic is a negative correlation between the temperature and the albedo with regard to rock units. This trend indicates the relation between the temperature and the albedo of rock types. High albedos (0.28–0.36) have low maximum temperatures (37–41 °C), whereas low albedos (0.17–0.24) have high maximum temperatures (44–47 °C). High and low albedos are associated with felsic and mafic rocks, respectively. This plot indicates that felsic rocks generally have high albedos and low temperatures, whereas mafic rocks generally have low albedos and high temperatures. The low albedos of mafic-to-ultramafic units give rise to high surface temperatures. Mafic-to-ultramafic units have higher temperatures because they absorb more solar radiation in the day time than other geological units due to their lower albedos. Thus, mafic-to-ultramafic units appear white in the ASTER L2 surface temperature image.

The second characteristic is the effect of vegetation density on albedo and temperature. The main data population for ASTER albedo and temperature forms a triangular shape (Figure 3.7). The high-albedo, low-temperature end member is a felsic unit, whereas the low-albedo, high-temperature end member is a mafic unit. The low-albedo, low-temperature end member indicates vegetation because dense vegetation has a low albedo and a low temperature. The densely vegetated area in Zimbabwe that is approximately 10 km north east from the Tati and Phoenix mines has the highest NDVI value (NDVI > 0.8) in the study area and this densely vegetated area has a low temperature (< 39 °C) in the L2 temperature image.

The third characteristic is a positive correlation between the albedo and the

temperature for moisture and water bodies. This correlation is observed for water bodies containing various amounts of water and for surface moisture. Water has a low albedo and a low temperature. A dammed reservoir has the lowest albedo (0.08–0.12) and temperature (23–25 °C) in the ASTER image of the study area. Areas with some moisture such as river banks are also plotted on this trend. River banks have high a NDVI (Figure 3.2 (f)), which indicates dense vegetation and gives a low albedo (Figure 3.2 (c)). River banks have a lower albedo and a lower temperature than densely vegetated areas due to the additional effect of water and moisture.

### 3.5.3 Spectral emissivity information in day time TIR data

Quartz exhibits a distinct spectral emissivity pattern in the TIR region due to Si–O stretching vibrations (Salisbury and Walter, 1989). Mafic-to-ultramafic rocks have gentle spectral emissivity patterns with emissivities in the range 0.70–1.00 (Figures 3.5 (a) and (b)), whereas quartz has a more distinctive spectral emissivity pattern with emissivities in the range 0.30–1.00 (Figure 3.5 (c)). This Reststrahlen feature of quartz also appears in the spectral emissivity patterns of quartz-bearing rocks such as granite (Figure 3.5 (d)), gneissic granite, and chert. Quartz and quartz-bearing felsic rocks appear reddish in the ASTER L1B day time TIR FCC image because quartz has a lower spectral emissivity in bands 10 and 12 than in band 14.

A ground truth survey confirmed that rock units that appear light red in the ASTER L1B day time TIR FCC image are muscovite schist and granite. The $SiO_2$ contents of these quartz-bearing rock units obtained by X-ray fluorescence analysis are 82.76 and 74.62 % $SiO_2$ for muscovite schist and 73.34 and 66.87 % $SiO_2$ for granite, which indicates the high quartz contents of these rocks.

Dry drainage regions (e.g., Ramokgwebana River, which flows along the Botswana–Zimbabwe border) appear bright red in the ASTER L1B day time TIR FCC image (Figure 3.2 (b)). Most rivers in Botswana are dry outside of the rainy season and appear as white or light yellow sand banks. Two river sand samples were analyzed by X-ray fluorescence analysis and gave $SiO_2$ contents of 86.59 and 72.25 %, demonstrating that the river sand is rich in quartz. The bright red of the river sand in the ASTER L1B day time TIR FCC image is due to its higher quartz content than general felsic rocks.

The quartz sand in dry drainage regions also appears red in the ASTER L2 day time TIR QI–CI–MI color composite image (R:G:B=QI:CI:MI), which indicates high QI values and low CI and MI values (Figure 3.3 (a)). The formula for QI enhances quartz-rich areas due to the spectral features of quartz in ASTER bands 10, 11, and 12 (Figure 3.5 (c)). However, it is generally difficult to discern the detailed features in the

QI image because the image is noisy (Figure 3.3 (b)). The noise of the QI image affects the ASTER L2 day time TIR QI–CI–MI color composite image. In addition, the grayscale QI image does not match well with the red regions in the ASTER L1B day time TIR FCC image (Figure 3.2 (b)). Moreover, high-value regions in the QI image match with areas that do not contain quartz, such as the mafic units around the Mupane Au mine and quartz-rich areas such as the granite unit around Shashe dam in the study area. To enhance imaging of quartz, we generated various band ratios of ASTER L2 day time emissivity data and found that a combination of bands 10, 11, and 12 generates a noisy image; this also occurs with bands 13 and 14 (Figure 3.3 (c)). This may occur due to bands 10–12 and bands 13 and 14 belonging to two groups of highly correlated data. Rockwell and Hofstra (2008) introduced the following quartz index based on bands 10–13 to enhance the spectral emissivity pattern of quartz:

Quartz index = (band 11/(band 10+band 12))*(band 13/band 12)

The QI image of Rockwell and Hofstra (2008) (Figure 3.8) generated by this formula using ASTER L2 day time emissivity data being less noisy than the QI image of Ninomiya et al. (2005), exhibits a good match with the red regions in the ASTER L1B day time TIR FCC image (Figure 3.2 (b)), and identifies quartz-rich fluvial sands along Ramokgwebana River. Using band 13 in the quartz index formula improves the quality of the quartz index image.

The MI image (Figure 3.3 (c)) does not clearly match the distribution of mafic-to-ultramafic units in the published geological map (Figure 3.2 (a)) nor the white regions in the ASTER L1B day time TIR FCC image (Figure 3.2 (b)). The MI image overestimates the distribution of mafic units and indicates areas around drainage as mafic units. Mafic units are not identified well in the MI image because the MI formula focuses on the spectral emissivity pattern of mafic rocks, which generally have more gentle patterns (Figure 3.5 (a)) than quartz (Figure 3.5 (c)). Because the plot diagram of Figure 3.6 indicates that the information of temperature dominates the emissivity in bands 13 and 14 of the ASTER day time TIR data, we conclude that the mafic-to-ultramafic units can be better identified from the temperature information than the spectral emissivity information.

Carbonate minerals have an emissivity feature caused by the vibration of $CO_3^{2-}$ in the TIR region at ASTER band 14. A CI image obtained from ASTER L2 TIR band 13/band 14 successfully delineated carbonate minerals at Nevada (Rockwell and Hofstra, 2008), but the CI image (Figure 3.3 (c)) could not be used to distinguish carbonate minerals in

the present study area. This may be because very few exposures of carbonate units are present in the study area (Figure 3.2 (a)). The spectral emissivity of carbonate minerals is weaker than that of quartz and may be difficult to distinguish in the ASTER L1B day time TIR FCC image due to the effect of temperature information.

The ASTER L1B day time TIR FCC image can be easily generated and provides a clearer color image for geological interpretation than the ASTER L2 TIR FCC image and other TIR index images (QI–CI–MI image) that have been proposed for geological mapping.

### 3.5.4 Effect of vegetation and land use on TIR data

The TIR FCC images and mineral index images are highly affected by the vegetation and land use of the surface. Granites with protruding topographic features and dense vegetation do not exhibit the features of quartz and appear light blue rather than pale red in the ASTER L1B TIR FCC image (Figure 3.2 (b)). The dark red regions do not indicate the quartz-rich unit distribution; rather they indicate agricultural areas from which vegetation has been removed. Agricultural areas exhibit significant spectral features of bare soil than untouched areas that are a mixture of rock, soil, and vegetation.

It is important to clarify the surface conditions of vegetation and land use by using ASTER VNIR FCC image obtained by respectively assigning R:G:B to band 3:band 2:band 1 because this image has higher spatial resolution (15 m) than the TIR image (90 m) and depicts vegetation in red. It is expected to be possible to clarify geological boundaries using this image. Accurate and advanced geological interpretation can be conducted by combining VNIR FCC images with TIR FCC image interpretation.

## 3.6 Conclusions

The ASTER L1B day time TIR FCC image (R:G:B=band 14:band 12:band 10) provides information regarding the spectral emissivity and temperature. Scatter plots of the ASTER L1B day time TIR digital values and ASTER L2 temperature indicate that bands 10, 11, and 12 contain spectral emissivity and temperature information, whereas the surface temperature dominates the spectral emissivity information in bands 13 and 14.

Mafic-to-ultramafic units appear white in the ASTER L1B day time TIR FCC image because they have higher surface temperatures than other units. The mafic-to-ultramafic units absorb more solar radiation due to their lower albedos and have a lower thermal inertia than other units (Pratt et al., 1978). Felsic units appear reddish in the ASTER

L1B day time TIR FCC image due to the distinct spectral emissivity of quartz. These geological units are important targets for platinum, gold, nickel, and copper in mineral exploration.

The proposed ASTER L1B day time TIR FCC images can be easily generated and provide a clearer color image for geological interpretation than ASTER L2 day time TIR FCC images and other TIR index images (QI, CI, and MI) that have previously been proposed for geological mapping.

Table 3.1 ASTER data used in this study

| ASTER Products | Acquisition date | Granule ID |
|---|---|---|
| L1B radiance | 2003, September 5 | ASTL1A 0309050829590309230137 |
| L2 emissivity (2B03) | Day time | ASTL1A 0309050830080309230138 |
| L2 temperature (2B04) | 2003, October 16 | ASTL1A 0310160824280310280332 |
| L2 reflectance (2B05V) | Day time | ASTL1A 0310160824370310280333 |
| L2 reflectance (2B05S) | 2005, October 12 | ASTL1A 0510120829380510150193 |
| | Day time | ASTL1A 0510120829470510150194 |
| | | ASTL1A 0510120829560510150195 |
| L1B radiance | 2008, May 11 | ASTL1A 0805112053220805160503 |
| | Night time | ASTL1A 0805112053310805160504 |

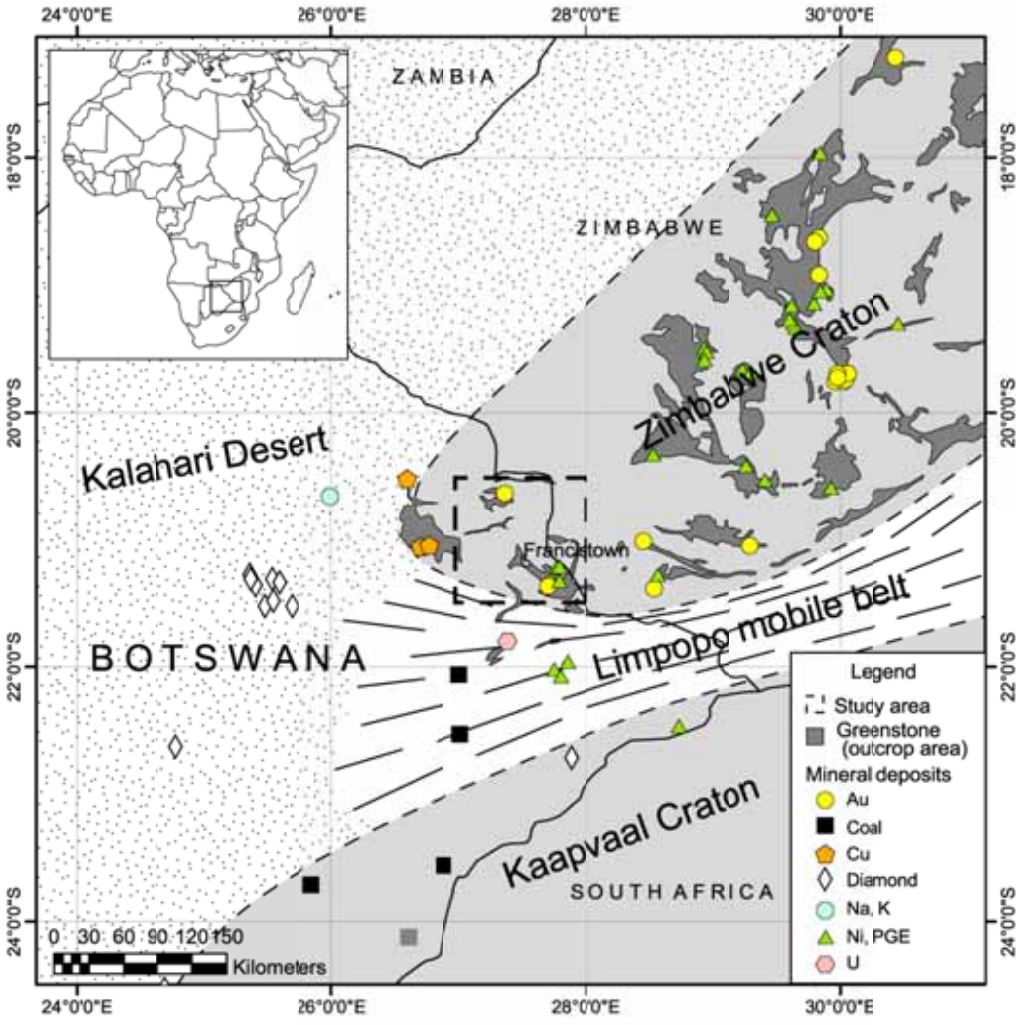


Figure 3.1 Regional geology and mineral occurrences of eastern Botswana (Modified from Machacha, 1997; Stagman, 1977; Baldock et al., 1976). The outcrop areas are limited to the eastern areas in Botswana.

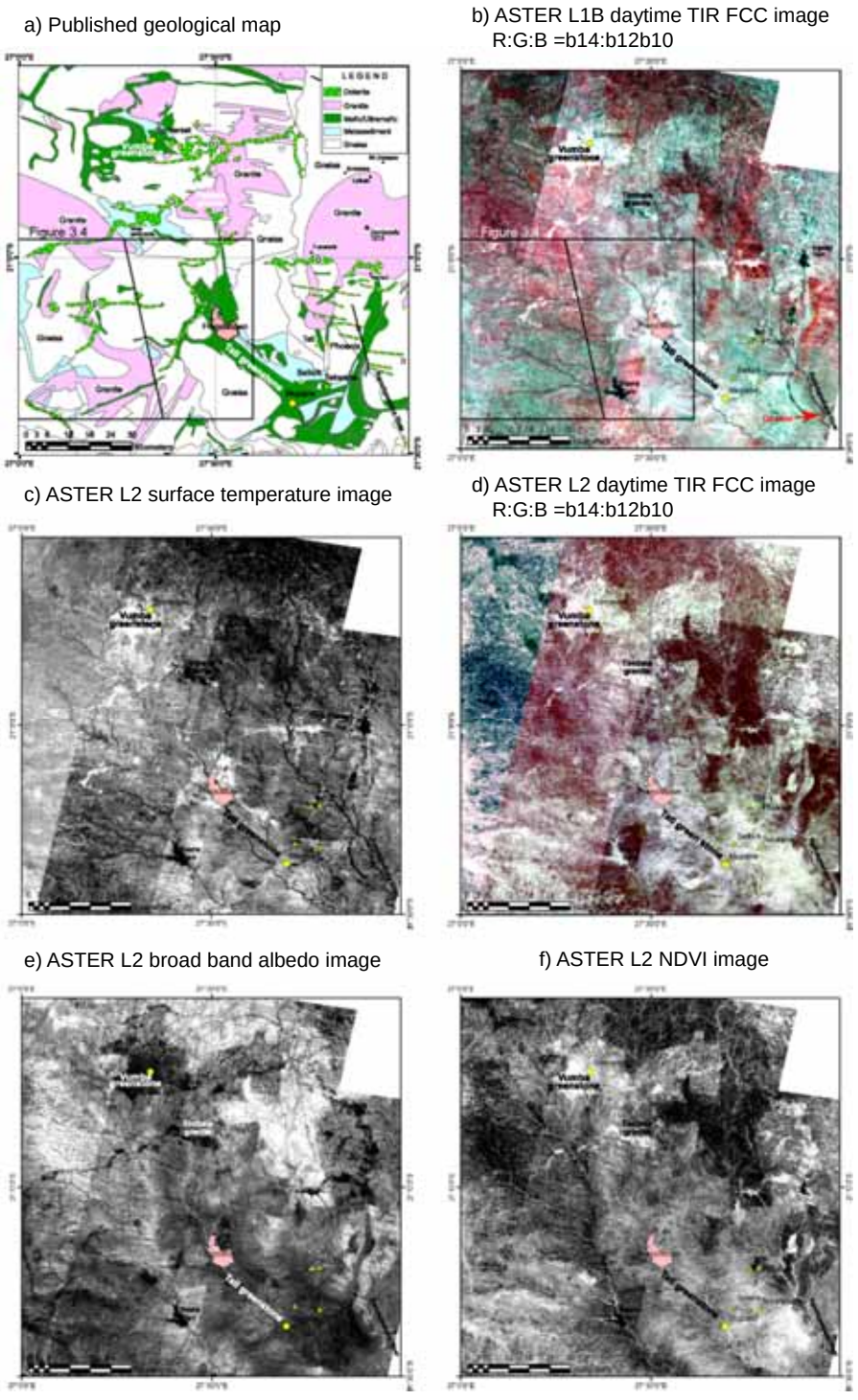


Figure 3.2 (a) Geological map of the study area (Modified from Key, 1976; Litherland, 1975; Aldiss, 1990). Green shows the distribution of mafic and ultramafic (M/UM) units and dolerite dykes. Pink shows the distribution of felsic granite units. (b) ASTER TIR FCC image (R:G:B = b14:b12:b10) using ASTER L1B daytime data. The M/UM units and dolerite dykes appear in white color. Quartz rich felsic units appear in

reddish color reflecting the amount of quartz. (c) ASTER surface kinetic temperature image using ASTER L2 temperature (2B03) data. The M/UM units and dolerite dykes appear white showing high surface temperature. (d) ASTER broadband albedo image (Liang, 2000) created from ASTER L2 reflectance data. The M/UM units and mafic dykes appear in dark tone due to dark color and low albedo.

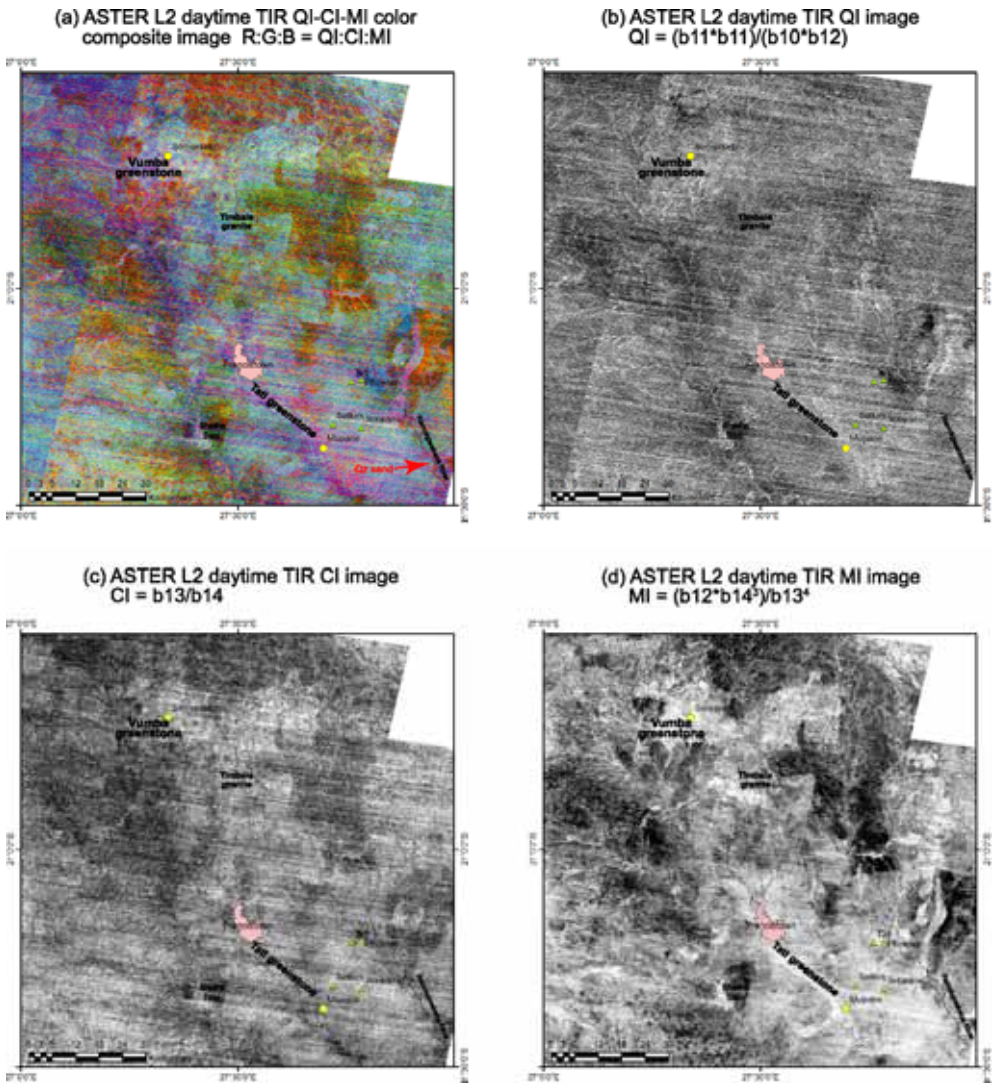


Figure 3.3 (a) ASTER TIR Quartz Index, Carbonate Index, Mafic Index color composite image (R:G:B = QI:CI:MI).created from ASTER L2 emissivity (2B04) data (Ninomiya et al., 2005). (b) QI gray scale image using ASTER L2 emissivity (2B04) data. The QI image contains high amount of noise. (c) MI gray scale image using ASTER L2 emissivity (2B04) data. (d) Band ratio (b14/b12) gray scale image using ASTER L2 emissivity (2B04) data to enhance quartz.

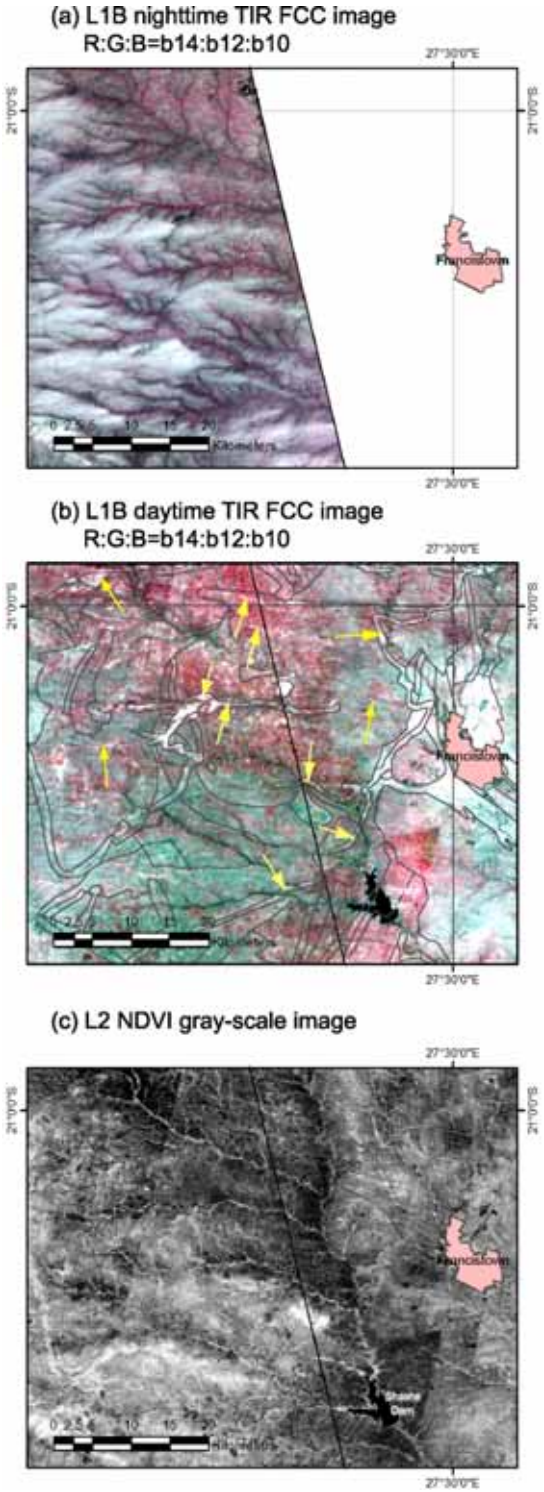


Figure 3.4 (a) ASTER TIR FCC image (R:G:B = b14:b12:b10) using nighttime L1B data. The area with white color shows the distribution of vegetation and lacks geological information. (b) ASTER TIR FCC image (R:G:B = b14:b12:b10) using daytime L1B data displays geological information. (c) NDVI image created from daytime ASTER L1B data showing the distribution of vegetation.

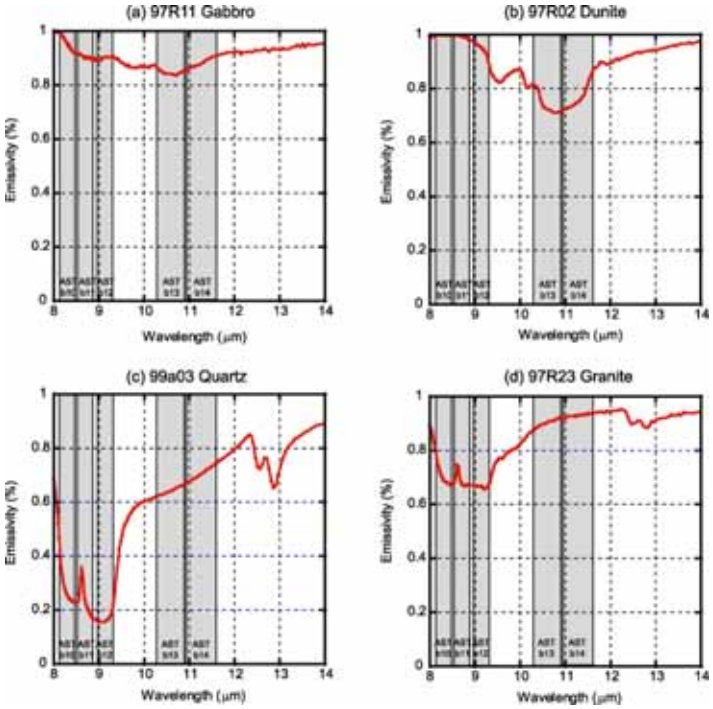


Figure 3.5 TIR spectral emissivity patterns of rocks and minerals. Quartz has a distinct spectral emissivity pattern (Modified after METI/MMAJ, 2001).

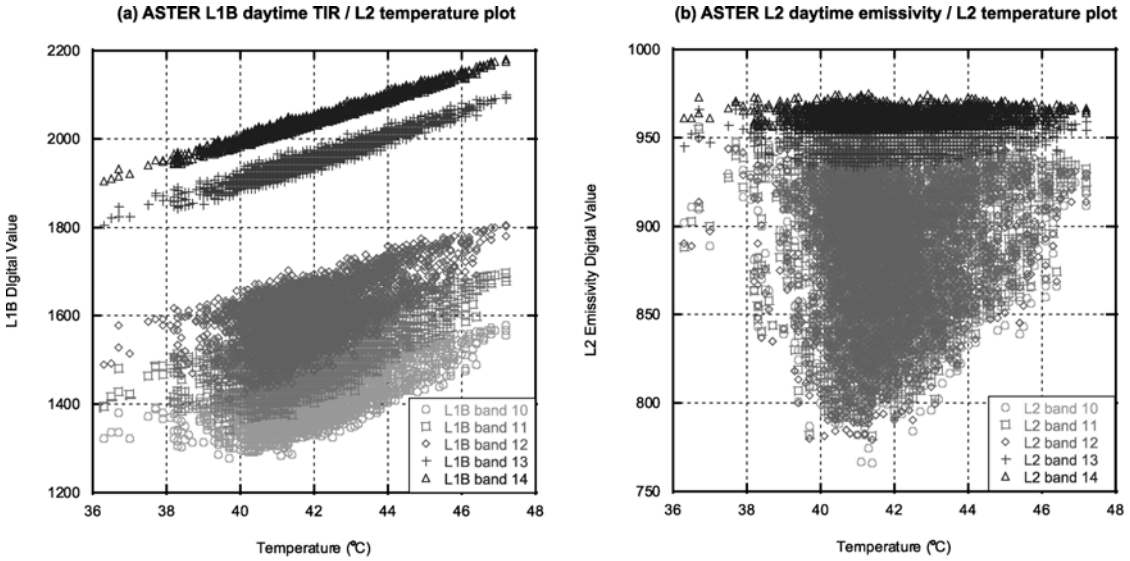


Figure 3.6 Plot diagram of ASTER TIR L1B digital values of the bands10 to 14 / ASTER L2 surface temperature (2B03) data. This plot clarifies that the bands 13 and 14 are highly correlated to temperature and the information of temperature dominates spectral emissivity. On the other hand, band 10, 11 and 12 are not highly correlated to temperature and provides information of both temperature and spectral emissivity.

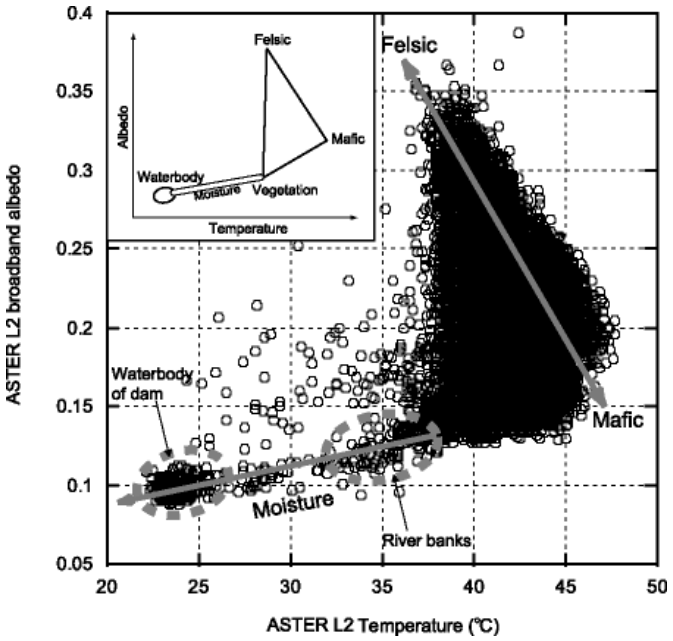


Figure 3.7 Plot diagram of albedo values derived from ASTER L2 reflectance data / ASTER L2 surface temperature (2B03). Two trends appear from this plot. The first trend is a negative correlation between the temperature and albedo of felsic and M/UM rocks. The second trend is a positive correlation that indicates amount of water or wetness.

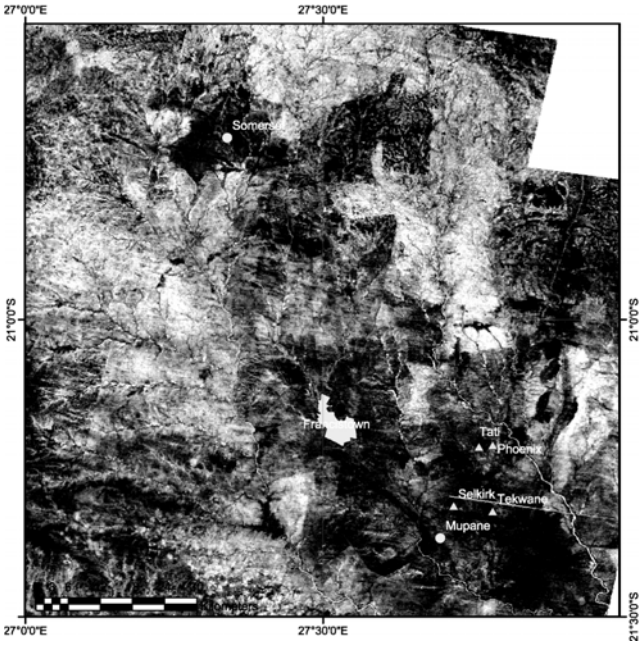


Figure 3.8 Quartz index image of Rockwell and Hofstra (2008) generated from ASTER L2 daytime emissivity data.

# CHAPTER 4

## Application of inverted slope images for geological mapping – reduction of artifacts in digital elevation models by filtering in the frequency domain

### 4.1 Introduction

Compared to other forms of remote sensing data, digital elevation models (DEMs) have not been used extensively for geological mapping. Rather, geological mapping has typically been performed using color composite images produced from multi-band sensor platforms, such as Landsat (Crosta and Moore, 1989) and Advanced Spaceborne Thermal Emission and Reflection Radiometer (ASTER) data (Hewson et al., 2005). However, DEMs have been used as subsidiary data to clarify linear or circular relief patterns for tectonic and structural analysis in geology (Masoud and Koike, 2006). Recently, studies using DEMs have increased, and DEMs have been used for landform mapping (Smith and Clark, 2005) and terrain classification (Iwahashi and Pike, 2007). DEM images that have been processed to show shaded relief and aspect have been used for geological mapping (Badura and Przybylski, 2005, Singh and Dowerah, 2010). In this paper, we describe the application of inverted slope images created from DEM images for geological mapping, and also propose a method to artifacts from image-derived DEMs.

A variety of spatial filtering (Brown and Bara, 1994) and frequency filtering (Hassan, 1988; Pan, 1989) methods have been developed to reduce the number of artifacts that are generated when DEMs are produced from contour lines. DEMs derived from remote sensing image data, such as the data collected by the Shuttle Radar Topography Mission (SRTM) (Rabus et al., 2003; Gesch et al., 2006) and Global DEM (GDEM) of the Advanced Spaceborne Thermal Emission and Reflection Radiometer (ASTER) (Fujisada et al., 2005; Tachikawa et al., 2011), currently almost cover the entire earth, and use of these image-derived DEMs currently exceeds that of contour-derived DEMs. Although contour- and image-derived DEMs have similar topography data, the processed DEM images, such as images with shaded relief and inverted slope images obtained from image-derived DEMs, are considerably noisier than those obtained from contour-derived DEMs. Consequently, reducing the artifacts in image-derived DEMs needs to be achieved in order to increase the potential application of image-derived DEMs, such as SRTM DEM and ASTER GDEM, to geological mapping.

## 4.2 Contour- and image-derived DEMs

A DEM is an ordered array of ground elevations at regularly spaced intervals. DEM data is originally point data consisting of latitude, longitude and altitude, but normally gridded to raster data. According to Guth (1999), DEMs can be divided into two groups depending on whether the source of data used to generate the DEM is (1) contour lines ("contour-derived DEM"), or (2) remote sensing imagery ("image-derived DEM").

Contour-derived DEMs are created from hypsographic maps produced by aerial photogrammetry and triangulation surveys. The height information in a contour-derived DEM is ground elevation data. Examples of contour-derived DEMs include the National Elevation Dataset (NED) of the United States, Canadian Digital Elevation Data (CDED), and the Japan Profile for Geographic Information Standards (JPGIS). Relatively few countries have accurate contour maps for public use and the availability of contour-derived DEMs is limited.

Image-derived DEMs are generated using remote sensing imagery and are not correlated with direct ground data. The height information in image-derived DEMs is canopy elevation. SRTM DEM and ASTER GDEM are typical image-derived DEMs with a near global coverage and are freely available.

NED DEM (a contour-derived DEM), and SRTM DEM and ASTER GDEM (image-derived DEMs) were used and compared in this study. Features of each DEM-type are shown in Table 4.1.

## 4.3 Study area

Cuprite in southwestern Nevada, approximately 200 km northwest of Las Vegas, was selected as the study area for geological mapping as the outcrop conditions are well and the geology, with its diverse hydrothermal alteration mineralogy, is well defined. Cuprite has been used extensively as a test site for a variety of remote sensing studies; particularly for extensive alteration mineral mapping exercises using AVIRIS data (Kruse, 2002), ASTER data (Rowan et al., 2003), Hyperion data (Kruse et al., 2003) have been conducted.

The regional geology of the Cuprite area has been described by Crafford (2007). Briefly, the area is composed of Lower Cambrian to Latest Proterozoic clastic rocks consisting of cross-bedded quartzite, siltstone, and phyllite (Czq) are underlain by Cambrian sedimentary units consisting of phyllite, schist, shale, thin-bedded limestone, chert, and siltstone (Ctd), which create the high northeast- to southwest-trending ridges that characterize the study area. Tertiary volcanic and sedimentary rocks, such as intermediate silicic ash flow tuff (Tt2), younger rhyolitic flows, and shallow intrusive

rocks (Tr3), younger silicic ash flow tuffs (Tt3), and younger tuffaceous sedimentary rocks (Ts3) are present over the lower sedimentary rocks and create gentle hills. Quaternary sediments, such as playa and floodplain deposits (Qpl) and alluvium (Qal) are present and cover the flat terrain (Figure 4.1).

## 4.4 Inverted slope images for geological mapping

A slope image is created using the steepest neighbor algorithm which is the maximum rate of change in value from the center to its neighbor cells (Guth, 1995). It is an approximate derivative of the original DEM. Gradient values in the slope image can be expressed in percent or degree units. The use of other algorithms, such as four or eight closest neighbors would change the values slightly, but would not change the resulting patterns.

For shaded relief images, sun illumination is from one direction only and some surface features are hidden by this orientation-effect. The flanks of Stonewall Mountain in the southeast of the study area are invisible in the shaded relief images because the direction of sun illumination is from the southeast (Figures 4.2 (a), (b), (c)). There is no orientation dependence in the slope images (Figures 4.2 (d), (e), (f)), but the lithology of the original slope image is difficult to interpret because the image is dark and the contrast is low. Consequently, detail of the topographic features was enhanced by inverting the slope image (Figures 4.2 (g), (h), (i)) to display the lithological units in a different tone and texture with stronger contrast.

In these inverted images, dark tones indicate outcrop areas with rigid terrain consisting of lithological units that are typically hard and resistant to weathering. White areas indicate flat or gently sloping terrain, such as talus areas covered by overburden and free of any outcrops. The inverted slope images provided considerable information on the distribution of lithological units. The clearest inverted slope image was obtained from contour-derived NED DEM data, while that obtained from GDEM data was extremely noisy.

## 4.5 DEM artifacts

Artifacts in the image-derived DEMs are both exaggerated and visible in the shaded relief and inverted slope images. Three types of artifacts were observed in the images used in this study (Figure 4.2, Figure 4.3).

1) Anomalous topographic features in the shaded-relief and slope images derived from the ASTER GDEM data in the eastern part of the study area (Figures 4.2 (c), (f), (i)). These anomalous features in the ASTER GDEM data were observed in

areas with low ASTER scene stack numbers, i.e., in areas with relatively few cloud-free images.

2) Fine-grained noise was extensive in the inverted slope images derived from SRTM DEM and ASTER GDEM data (Figures 4.2 (h), (i)). The random noise observed in the ASTER GDEM inverted slope image was more intense than that observed in the SRTM DEM data, and the noise obscured topographic information. However, these random artifacts were uniformly present in the SRTM DEM and ASTER GDEM data (Figures 4.3 (b), (c)). In addition, the magnitude of the random noise was small in the topographic section, but markedly higher in the slope sections (Figures 4.3 (e), (f)).
3) Single-point spike-type errors were observed in the topographic sections of the ASTER GDEM data (Figure 4.3 (c)); these errors are typically difficult to perceive in both shaded-relief images and inverted slope images (Figures 4.3 (c), (f)).

Contour-derived NED DEM images had fewer artifacts compared to the image-derived DEM images, but they were not completely free of artifacts. For example, artifacts referred to as contour "ghosts" were observed in imagery of the northwestern part of the study area in both the shaded-relief and inverted slope images (Figures 4.2 (a), (d), (g)). Contour "ghosts" are associated with the contour to grid algorithm producing grid-node elevations with the same elevation (Guth, 1999). They are small artifacts and do not appear as elevation errors in the topographic and slope sections. Collection line artifacts, which produce stripes or aligned textures in USGS 7.5 minute DEM data, have been reported (Albani and Klinkenberg, 2003), but no such artifacts were observed in this study area.

Image-derived DEM data contains more artifacts than the contour-derived DEMs generally. Reducing artifacts from image-derived DEMs is therefore considered important for obtaining smooth topographic information. Although SRTM DEM and ASTER GDEM both contain artifacts that can be attributed to topographic information, it is clear that ASTER GDEM contains more artifacts than SRTM DEM.

## 4.6 Artifact reduction methods

Spatial filters are effective for reducing spike-type errors in a DEM, but if spatial filtering is applied to an entire DEM, it will decrease the spatial resolution and diminish the detailed features of all of the original DEM information. The application of spatial filters should therefore be restricted to spike-type artifacts.

When using multiband remote sensing data, valid elevation information can be

distinguished from artifacts by performing a principal components analysis (PCA) or maximum noise fraction (MNF) transformation (Green et al., 1988), which will separate information and artifacts into different PCA clusters (Crosta and Moore, 1989; Loughlin, 1991) or MNF bands (Kruse et al., 2003). Artifact reduction can then be achieved by deleting those bands dominated by noise, and then reverting back to the PCA or MNF data; however, PCA and MNF analyses cannot be applied to single band data.

Fast Fourier transformation (FFT) can reduce artifacts from single band data and FFT has been employed to reduce systematic artifacts from remote sensing images (e.g., de Souza Filho et al., 1996). Figure 4.4 shows a flow chart describing the process for reducing artifacts from DEMs. Briefly, spatial data is transformed into the frequency domain by FFT. Intrinsic image and elevation information is concentrated at low frequencies which are located at the center of the FFT frequency image (Figure 4.5 (a)) creating a peak and troughs representing the high frequency information which contains very fine textured information and noise (Figure 4.5 (b)). Specific high-frequency artifacts in the image-derived DEMs can then be removed by applying a low-pass filter of a specific size to the FFT frequency data (Figure 4.5 (c)). After filtering the high frequency components using the low-pass filter, an inverse FFT transforms the frequency image back to the image domain. Random artifacts are uniformly distributed from the low to high frequency components of the frequency image (Hassan, 1988). Although FFT filtering cannot entirely remove these random artifacts, the artifacts at low frequencies will be dominated by more signal and/or information that is intrinsic to the image making the artifacts less recognizable.

## 4.7 Discussion

Inverted slope images, such as that shown in Figure 4.2 (g), clearly show areas of outcrops and provide even more information of the differences in lithological units when compared to published geological maps (Figure 4.1). However, the inverted slope images created from image-derived DEMs (especially ASTER GDEM) are typically very noisy (Figures 4.2 (h), (i)). This happens because the image-derived DEM contains artifacts that do not reflect the true topography, especially since artifacts are frequently produced when DEMs are generated. While most of the artifacts in the original image-derived DEMs are difficult to recognize, they are typically exaggerated as noise in the inverted slope images. Detailed information of landforms and lithology is often hidden by this noise.

ASTER GDEM is particularly noisy in low-relief areas because image correlation is more difficult to accomplish in images of flat terrains (Fujisada et al., 2005). Reducing

artifacts from ASTER GDEM is essential because, compared to NED and SRTM DEM, more noise appears in inverted slope images produced from ASTER GDEM data.

FFT transforms the DEM data into the frequency domain, with a range of high to low frequency components. Although it is possible to filter specific frequencies from the FFT frequency image, excessive filtering will remove original topographic information. The optimum filter size is thus one that minimizes the loss of topographic information while maximizing the removal of artifacts.

An exponential circle filter was used for low-pass filtering because an ideal circle filter truncates the cutoff frequency and produces ripple like phenomena (Oppenheim and Schafer, 1970). FFT frequency filtering at twelve low-pass filter sizes (1 %, 5 %, 10 %, 20 %, 30 %, 40 %, 50 %, 60 %, 70 %, 80 %, 90 %, 100 %) was applied to the original SRTM DEM and ASTER GDEM data (Figure 4.5 (c)). Using a small low-pass filter size maintains the very lowest frequency components and removes the large residue associated with the higher frequencies (Figure 4.5 (d)). Shaded and inverted slope images produced using FFT-filtered SRTM DEM data (Figure 4.6) and FFT-filtered ASTER GDEM data (Figure 4.7). It was found that the amount of noise in the images decreased with the size of the low-pass filter, but the spatial resolution of the images also decreased and the image became smoother. Changes in noise and terrain resolution associated with FFT filtering were more apparent in inverted slope images than in shaded relief images.

In order to determine optimum filter size, the differences between mean NED DEM, FFT-filtered SRTM DEM and ASTER GDEM values at different low-pass filter sizes was computed and plotted in Figure 4.8. A specific filter showing the minimum artifact size relative to the most topographic information for the filtered DEM was not obtained, but a trend approximating the optimal filter size was clarified. As the size of the low-pass filter was decreased, the number of artifacts in the DEM was reduced, but, as a tradeoff, some of the original topographic information was also lost. For both SRTM DEM and ASTER GDEM data, artifact reduction was constant when the low-pass filter size exceeded 40 %; at filter sizes of less than 20 %, the loss of artifact and topographic information increased. Thus, a filter size of 20 to 40 % was considered optimal for maximizing artifact reduction while reducing the loss of topographic information in this study. No significant difference was observed in assessments of optimum filter size in both SRTM DEM and ASTER GDEM data.

Topographic and slope sections of FFT-filtered SRTM DEM and ASTER GDEM data transformed using a filter size of 30 % are shown in Figure 4.9. Random artifacts present in the original SRTM DEM and ASTER GDEM data (Figures 4.3 (b), (c)) were

generally reduced (Figures 4.9 (a), (b)), but the DEM artifacts associated with cloud occurrence in the GDEM data persisted in the flat areas. These single-spike errors need to be removed by selective spatial filtering. The slope sections obtained from the original SRTM DEM and ASTER GDEM data could not be interpreted as being the same terrain (Figures 4.3 (e), (f)). However, when the same slope sections of SRTM DEM and ASTER GDEM data were transformed using a filter size of 30 %, the resulting topology was comparable with the same areas in the NED DEM images (Figure 4.3 (d), Figures 4.9 (c), (d)).

## 4.8 Conclusions

Inverted slope images show differences in lithology more clearly than images of the same areas showing only the shaded relief. While inverted images are useful for geological mapping, artifacts in the image-derived DEM data give the images a noisy texture and obscure information related to lithological units. Although the artifacts in the SRTM DEM and ASTER GDEM data are typically minor and unrecognizable in the original topographic data, they become exaggerated in the inverted slope images and produce images with a noisy texture. We attempted to reduce the artifacts in image-derived DEMs by FFT filtering and successfully removed high to medium-low frequency artifacts in the frequency image. Specifically, low-pass filtering using an exponential circle filter with a size of 20 to 40 % effectively reduced the artifacts without a significant loss of terrain information from the image-derived DEMs in the study area.

Compared to SRTM DEM, inverted ASTER GDEM images of flat terrain had high levels of noise which obscured the underlying topographical information. It is therefore necessary to reduce artifacts from ASTER GDEM data before creating shaded relief or slope images. Inverted slope images created from artifact-reduced DEM data subjected to FFT filtering can facilitate the accurate classification of lithological variation and rock composition.

Table 4.1 Contour-derived DEM and image-derived DEM used for the study.

| | NED | SRTM (SRTM1) | ASTER GDEM (GDEM2) |
|---|---|---|---|
| DEM type | Contour-derived DEM | Image-derived DEM | Image-derived DEM |
| Data provider country | USA | USA | Japan |
| Horizontal grid spacing | 1 arc second | 1 arc second | 1 arc second |
| Coverage | Contiguous US, Hawaii and Puerto Rico (Except for Alaska) | Contiguous US, Hawaii and Puerto Rico (Alaska to 60° N) | 83° N to 83° S |
| Data source | Aerial photos | C-band SAR | ASTER VNIR band3N/B |
| DEM production | Contour to grid | Interferometry | Stereography |

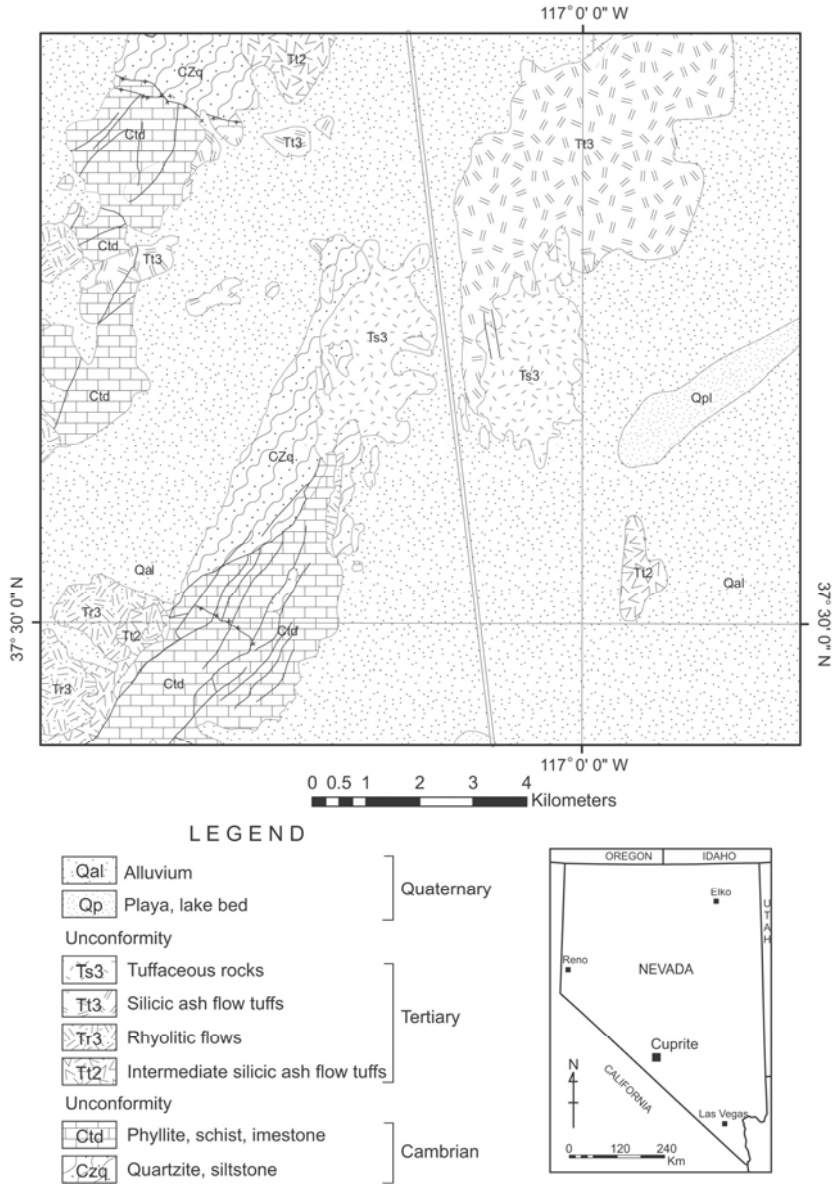


Figure 4.1 Geological map of the study area (modified after Crafford, 2007).

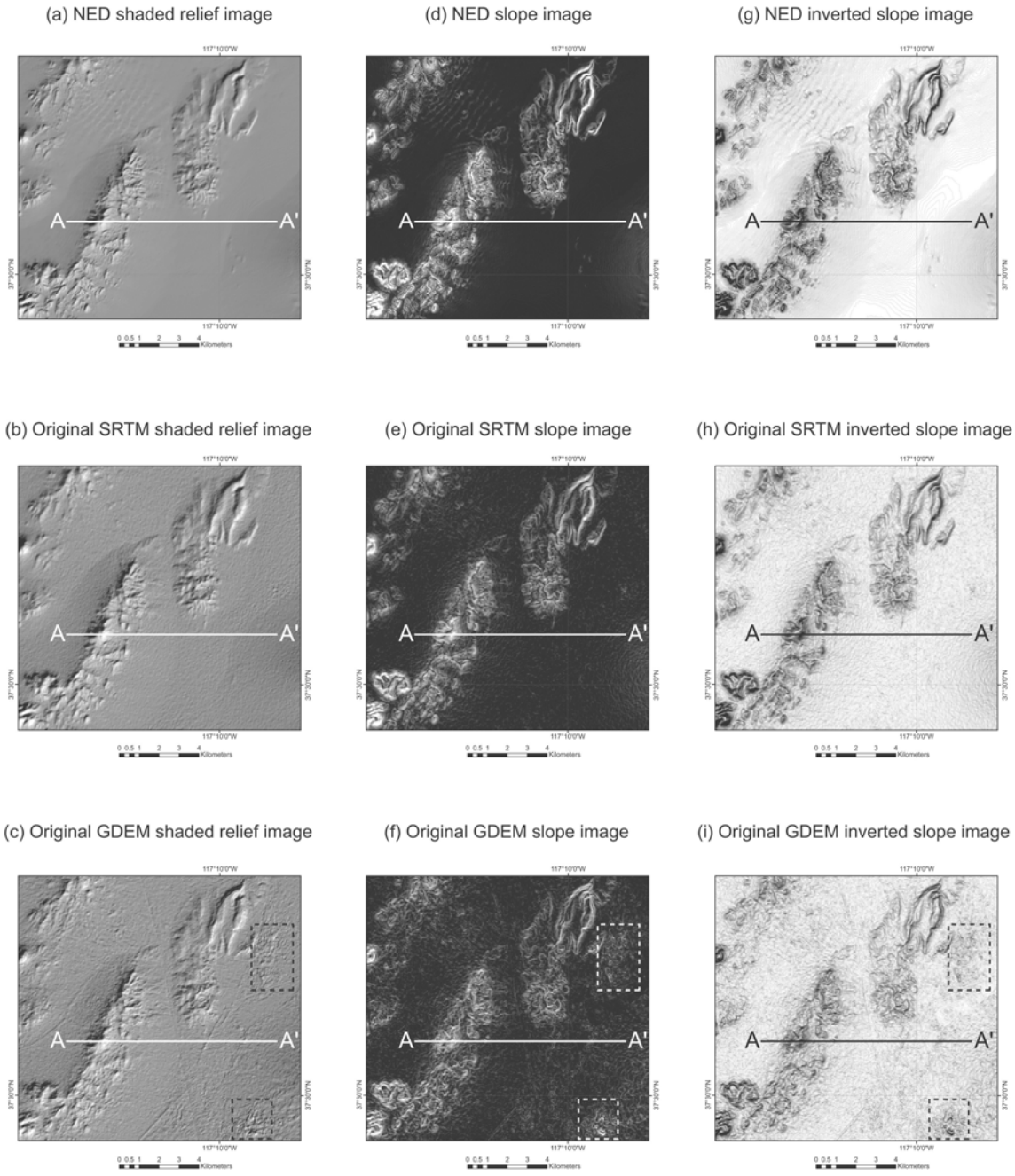


Figure 4.2 Shaded relief images, slope images and inverted slope images of the study area.

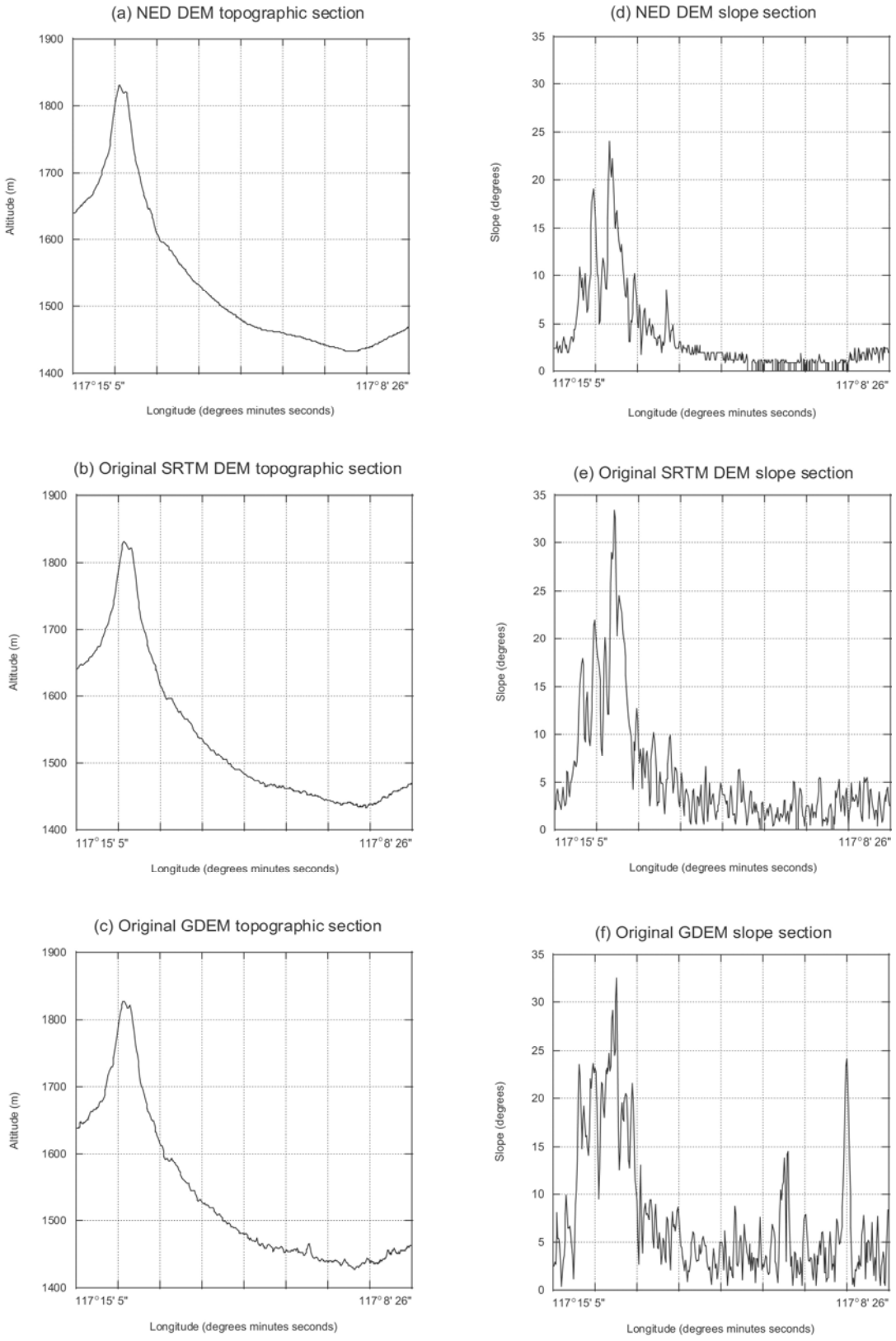


Figure 4.3 DEM topographic sections and DEM slope sections of line A-A' in figure 4.2.

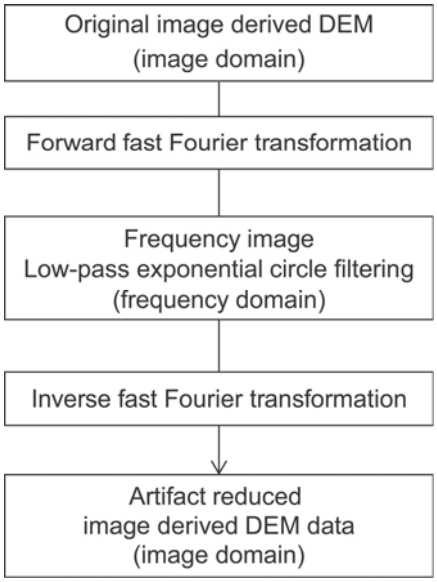


Figure 4.4 Flow chart for reducing artifacts from DEM data.

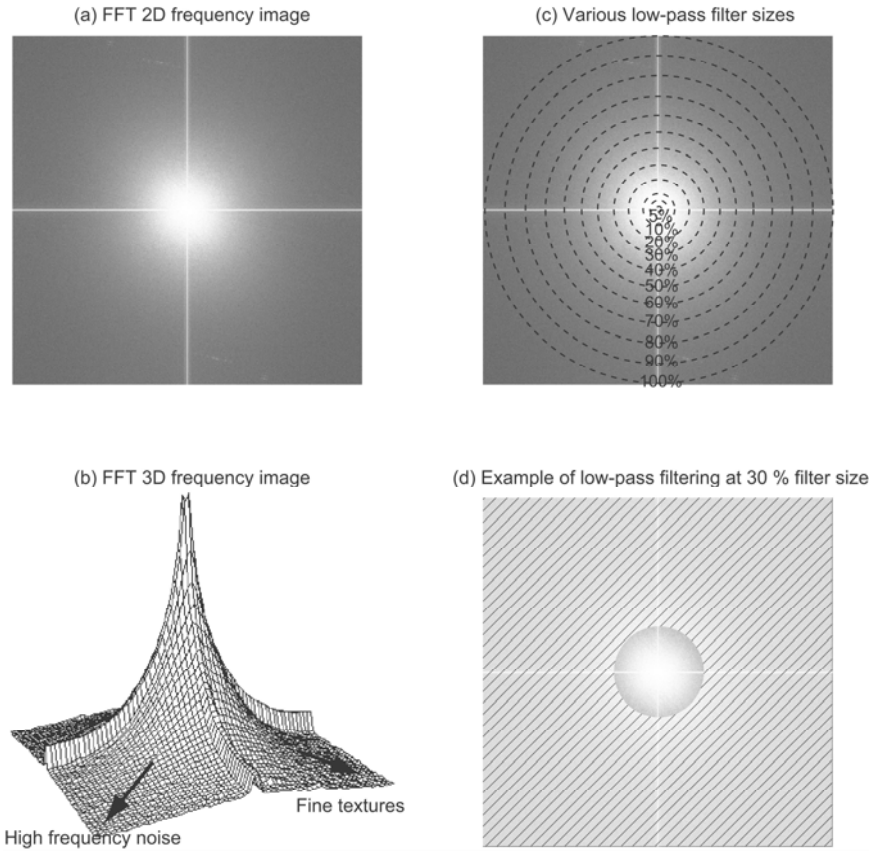


Figure 4.5 FFT frequency images and low-pass filter sizes.

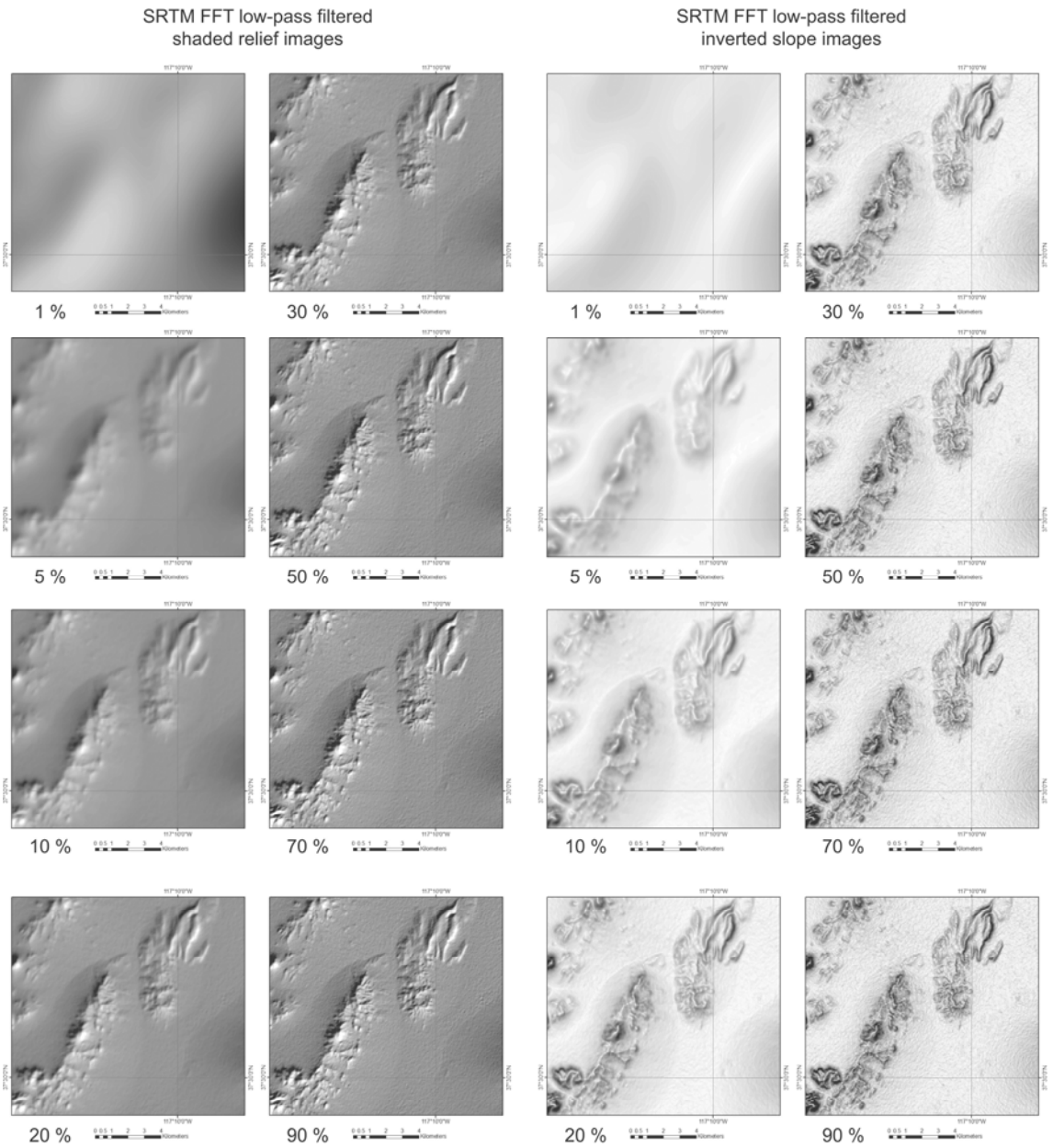


Figure 4.6 SRTM DEM FFT filtered shaded relief images and inverted slope images of different low-pass filter sizes.

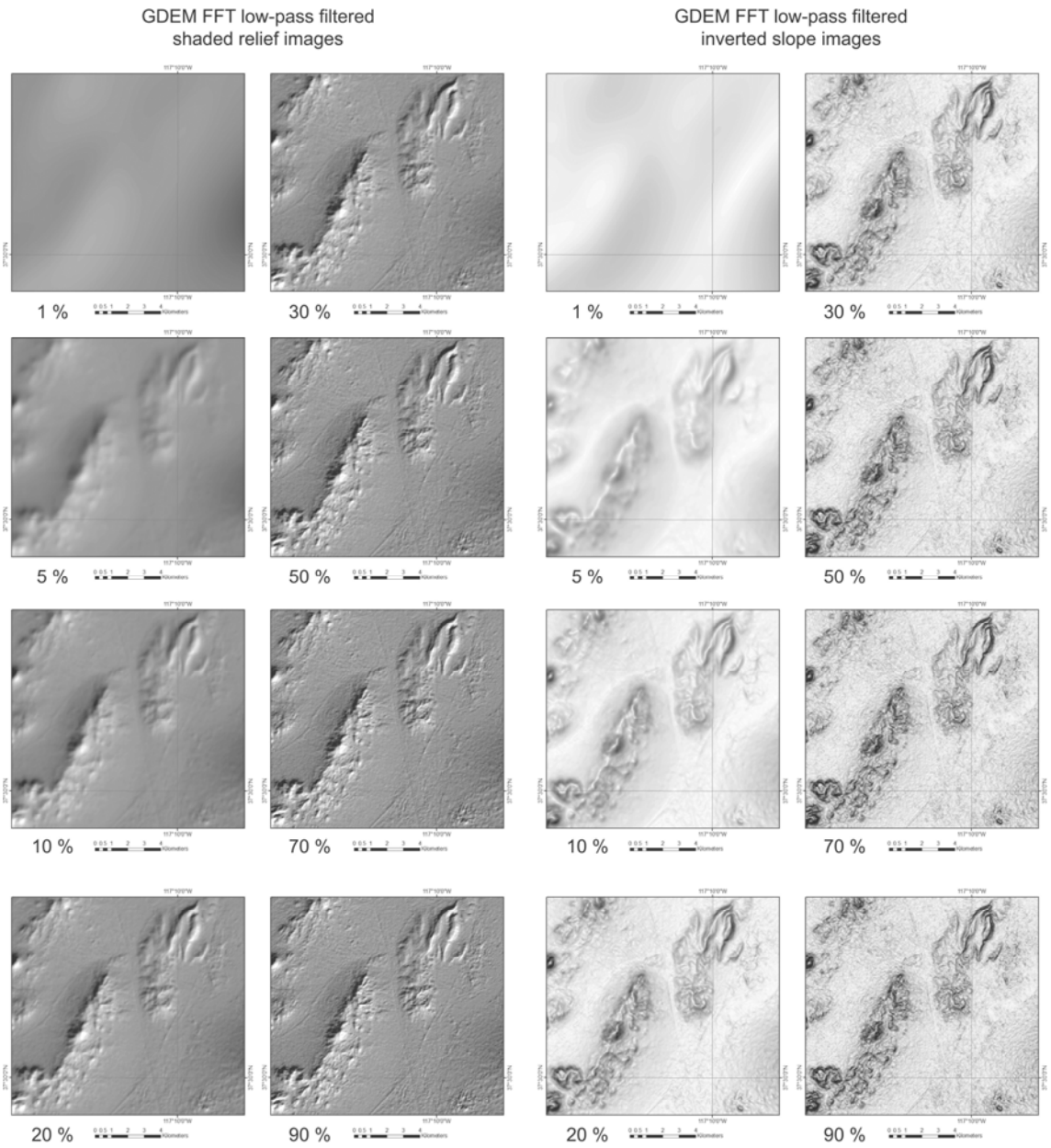


Figure 4.7 GDEM FFT filtered shaded relief images and inverted slope images of different low-pass filter sizes.

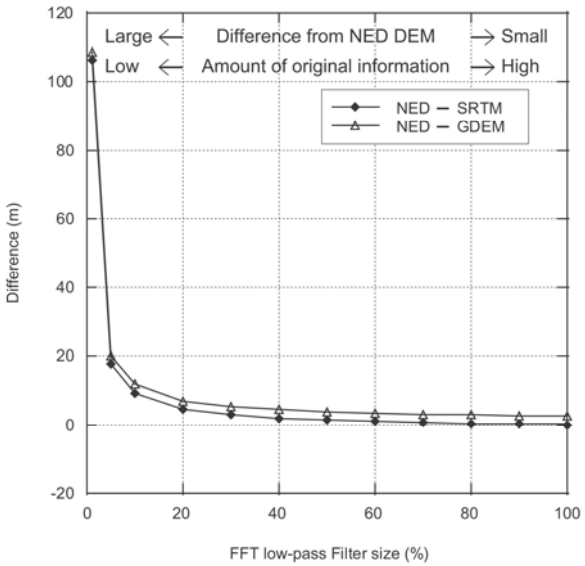


Figure 4.8 Difference of mean values between NED DEM and FFT filtered image derived DEM data at various low-pass filter sizes.

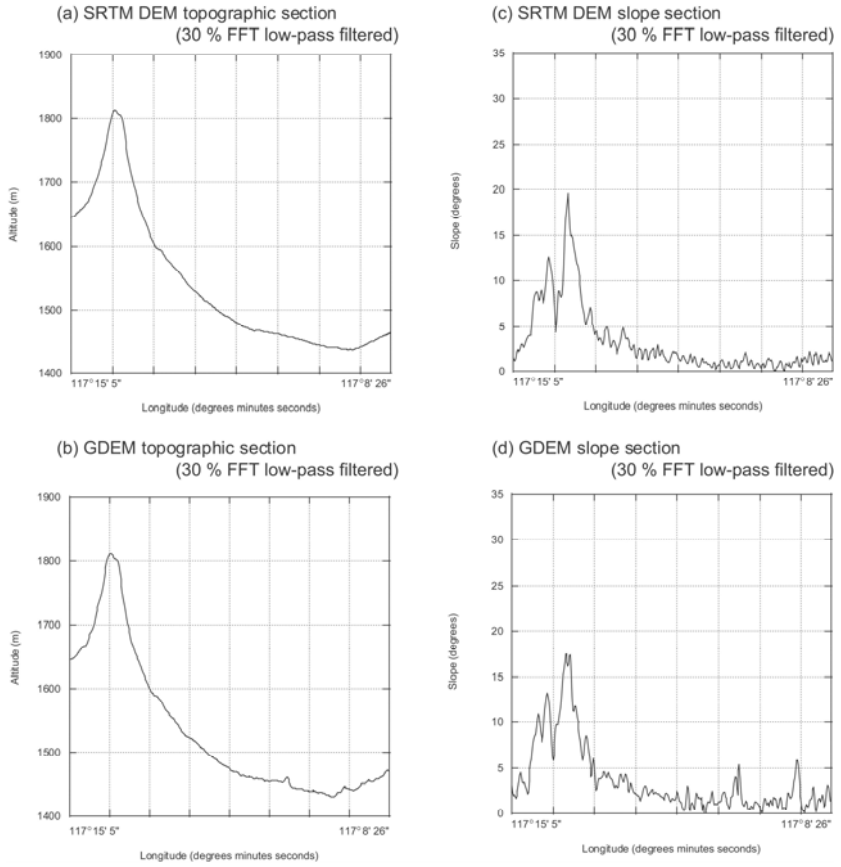


Figure 4.9 Topographic section and slope section of 30 % FFT low-pass filtered DEM.

# CHAPTER 5

## Conclusions

The processing methods and applications of ASTER data for mineral resources exploration and geological mapping were studied in this thesis.

(1) Alteration mapping using ASTER VNIR and SWIR data

Alteration zones are important features for the exploration of porphyry copper deposits. The ASTER sensor is able to identify the types of alteration and its alteration zoning, which are important information for mineral resource exploration. The utilization of three processing methods are described, 1) SWIR false color image, 2) band ratio color composite image, and 3) principal component analysis (PCA) color composite image.

The SWIR false color image is a false color image using band 4, band 6 and band 8 (R:G:B=band 4:band 6:band 8). The alteration zones appear as pink or green colors in the alteration image.

The band ratio color composite image uses the band ratio images of band 4/band 6, band 5/band 6 and band 5/band 8 (R:G:B=band 4/band 6:band 5/band 6:band 5/band 8). The band ratio image is able to provide information of the alteration zoning. Band 4/band 6 enhances the advanced argillic alteration, band 5/band 6 enhances the phyllic alteration and band 5/band 8 enhances the propylitic alteration.

The PCA image ("Crosta technique") is also able to provide information of the alteration zoning. The PCA color composite image consists of the PCA alteration images that are obtained from three PCA processes (R:G:B=PCA advanced argillic alteration image: PCA phyllic alteration image: PCA propylitic alteration image). The advanced argillic alteration image is obtained from PCA of band 1, band 4, band 6 and band 7, the phyllic alteration image is obtained from PCA of band 1, band 3, band 5 and band 6 and the propylitic alteration image is obtained from PCA of band 1, band 3, band 5 and band 8. The PCA alteration images are chosen by checking the eigen vectors.

These methods are applied to the Meiduk area of Iran, which is known for porphyry copper mineralizations. Combinational use of the images enables identification of the hydrothermal alteration and zonings related to porphyry copper mineralization.

(2) Geological mapping using ASTER TIR data

Geological units are identified by using ASTER TIR data, which contains both

surface temperature and spectral emissivity information. A scatter plot of ASTER L1B day time TIR digital values and L2 day time temperature indicates that in the ASTER L1B day time TIR data, bands 10, 11, and 12 contain spectral emissivity and temperature information, whereas surface temperature dominates the spectral emissivity information in bands 13 and 14. Visual interpretation of the ASTER TIR false color images generated by assigning band 14, band 12 and band 10 (R:G:B=band 14:band 12:band 10) using L1B day time data allowed to identify mafic-to-ultramafic units and quartz-rich felsic units. Mafic-to-ultramafic units such as gabbro, dolerite, and dunite appear white in ASTER L1B day time TIR false color images due to their high spectral emissivities in the 8–9 μm region (bands 10 and 12) and high surface temperatures. Mafic-to-ultramafic units have higher surface temperatures than other geological units because they absorb more solar radiation due to their lower albedos and they have a lower thermal inertia. Quartz-rich felsic units such as granite and dry river sand appear reddish in the ASTER L1B day time TIR false color image because the spectral emissivity of quartz is lower in the 8–9 μm region (bands 10 and 12) than in the 10–12 μm region (band 14). Mafic-to-ultramafic and granitic units are important targets for mineral exploration because they are potential geological units to host or accompany mineralization. The proposed ASTER L1B day time TIR false color images can be prepared very simply and they provide valuable information for geological mapping and mineral exploration.

(3) Geological mapping using ASTER GDEM data

Inverted slope images created from DEMs can be used to visualize differences in lithological units and provide an indication of areas of geological outcropping. Such images are useful for geological mapping, but when created from DEMs generated from remote sensing images (“image-derived DEMs”), artifacts in the DEMs are exaggerated and give rise to unclear noisy final images. Such artifacts also affect the quality of normal slope images and shaded relief images. In contrast, DEMs created from elevation data in the form of contour maps (“contour-derived DEMs”) contain far fewer artifacts, but their availability is limited. Therefore, in order to obtain clear processed DEM images that can be used for global geological mapping, it is necessary to develop a method for reducing the number of artifacts in image-derived DEMs.

In the present study, the effectiveness of a fast Fourier transform (FFT) for artifact reduction in image-derived DEMs was investigated. The FFT converts spatial data into the frequency domain, and artifacts with specific frequencies are removed by low-pass filtering. An inverse FFT is then used to return to the spatial domain, thus producing a

filtered DEM with a reduced number of artifacts. The effect of the filter size on the final image quality was also investigated.

The image-derived DEMs used in this study were the Shuttle Radar Topography Mission (SRTM) DEM and the ASTER GDEM for Cuprite, Nevada. A comparison was made between shaded relief and inverted slope images created following artifact removal from these DEMs and equivalent images produced using the contour-derived National Elevation Dataset (NED) DEMs. It was clarified that for the image-derived DEMs, that a low-pass filter with a size of 20 to 40 % significantly reduced the number of artifacts without significant loss of terrain information. For the ASTER GDEM data, artifact reduction was found to be particularly important because the artifacts obscure the original topographic information in the inverted slope images.

Combinational use of the proposed methods is recommended for more accurate interpretation of remotely sensed images for the purposes of mineral exploration and geological mapping. When conducting alteration mapping for exploration, it is important to know whether the alteration information is from an outcrop area and not from a talus area. Inverted slope images produced from DEM data is able to provide information identifying outcrop areas. TIR data are affected by surface conditions such as vegetation or land use (agricultural or grazing areas). VNIR data are important for clarifying the surface conditions in TIR 14-12-10 FCC images. Accurate lithological mapping can be performed by combining VNIR FCC and TIR 14-12-10 FCC images.

The proposed methods in this study are simple but useful and provide reproducible results. The images could be used widely by geologists or geophysicists involved in mineral resources exploration. ASTER VNIR and SWIR data have been widely used in exploration for alteration mapping mainly targeting hydrothermal ore deposits that accompany alteration minerals, and this study has also considered the ability of ASTER TIR and GDEM data for use in geological mapping and its effectiveness for exploration of magmatic ore deposits.

# REFERENCES


Abrams, M.J., Kahle, A.B., Palluconi, F.D., Schieldge, J.P., 1984, Geologic mapping using thermal images. Remote. Sens. Environ., 16, 13–33.

Albani, M. and Klinkenberg, B., 2003, A Spatial Filter for the Removal of Striping Artifacts in Digital Elevation Models. Photogrammetric Engineering & Remote Sensing, 69, 755–765.

Badura, J. and Przybylski, B., 2005, Application of digital elevation models to geological and geomorphological studies – some examples. Przeglàd Geologiczny, 53(10), 977-983.

Bagai, Z., Armstrong, R.A., and Kampunzu, A.B., 2002, U-Pb single zircon geochronology of granitoids in the Vumba granite-greenstone terrane (NE Botswana): Implications for the evolution of the Archean Zimbabwe craton. Precambrian Research, 118, 149-168.

Baldock, J.W., Hepworth, J.V.,Marengwa, B.S., 1976, Gold, basemetals, and diamonds in Botswana. Economic Geology, 71, 139–156.

Barnes, S.J. and Lightfoot, P.C., 2005, Formation of Magmatic Nickel Sulfide Deposits and Processes Affecting Their Copper and Platinum Group Element Contents. Economic Geology 100$^{th}$ Anniversary Volume, 179-213.

Brown, D.G. and Bara, T.J., 1994, Recognition and Reduction of Systematic Error in Elevation and Derivative Surfaces from 7.5-minute DEMs. Photogrammetric Engineering and Remote Sensing, 60, 189-194.

Carney, J.N., Aldiss, D.T., Lock, N.P., 1994, The geology of Botswana. Geological Survey of the Botswana Bulletin 37, pp. 1-113.

Clark, R.N., Swayze, G.A., Wise, R., Livo, K.E., Hoefen, T.M., Kokaly, R.F. and Sutley, S.J., 2002, USGS Digital Spectral Library splib05a, USGS Open File Report 03-395.

Crafford, A.E.J., 2007, Geologic Map of Nevada. U.S. Geological Survey Data Series 249, 46.

Crippen, R.E., 1989, Selection of Landsat TM band and band-ratio combinations to maximize lithologic information in color composite displays, Proceedings of the 7th ERIM Thematic Conference on Remote Sensing for Exploration Geology, 917-921.

Crosta, A.P. and Moore, J.McM., 1989, Enhancement of Landsat Thematic Mapper imagery for residual soil mapping in SW Minas Gerais State Brazil: a prospecting case history in greenstone belt terrain. Proceedings of the 9th Thematic Conference on Remote Sensing for Exploration Geology, Calgary (Ann Arbor, MI: Environmental Research Institute of Michigan), 1173-1187.

Crosta, A.P., Souza Filho, C.R., Azevedo, F. and Brodie, C., 2003, Targeting key alteration minerals in epithermal deposits in Patagonia, Argentina, Using ASTER imagery and principal component analysis, International Journal of Remote Sensing, 24 (21), 4233-4240.

De Souza Filho, C.R., Drury, S.A., Denniss, A.M., Carlton, R.W.T., and Rothery, D.A., 1996, Restoration of Corrupted Optical Fuyo-1 (JERS-1) Data Using Frequency Domain Techniques. Photogrammetric Engineering and Remote Sensing, 62, 1037-1047.

Earth Resource Data Analysis Center (ERSDAC), 2001, ASTER users guide Ver. 3.0.

Earth Resource Data Analysis Center (ERSDAC), 2003, The major cities of the world, ASTER image library 2.

Fiorentini, M.L., Bekker, A., Rouxel, O.,Wing, B.A., Maier,W., Rumble, D., 2012, Multiple sulfur and iron isotope composition of magmatic Ni–Cu–(PGE) sulfide mineralization from Eastern Botswana. Economic Geology, 107, 105–116.

Fraser, S.J., 1991, Discrimination and identification of ferric oxides using satellite Thematic Mapper data: a Newman case study. Int. J. Remote Sens., 12, 635–641.

Fujisada H., Bailey G.B., and Kelly G.G., 2005, ASTER DEM Performance. IEEE Transactions on Geoscience and Remote Sensing, 43, 2707-2714.

Gesch, D.B., Muller, J.P., and Farr, T.G., 2006, The Shuttle Radar Topography Mission – Data Validation and Applications. Photogrammetric Engineering and Remote Sensing, 72, 233-235.

Gillespie, A., Kahle, A.B., Palluconi, F.D., 1984, Mapping alluvial fans in Death Valley, California, using multichannel thermal infrared images. Geophys. Res. Lett., 11, 1153–1156.

Gillespie, A., Rokugawa, S., Matsunaga, T., Cothern, J.S., Hook, S., Kahle, A.B., 1998, A temperature and emissivity separation algorithm for Advanced Spaceborne Thermal Emission And Reflection Radiometer (ASTER) images. IEEE Trans. Geosci. Remote Sens., 36, 1113–1126.

Goetz, A.F.H., Rowan, L.C., 1981, Geologic remote sensing. Science, 211, 781–791.

Green, A.A., Berman, M., Switzer, P., and Craig, M.D., 1988, A Transformation for Ordering Multispectral Data in Terms of Image Quality with Implications for Noise Removal. IEEE Transactions on Geoscience and Remote Sensing, 26, 65-74.

Guth, P.L., 1995, Slope and aspect calculations on gridded digital elevation models: Examples from a geomorphometric toolbox for personal computers. Zeitschrift fir Geomorphologie, 101, 31-52.

Guth, P.L., 1999, Contour Line “Ghosts” in USGS Level 2 DEMs. Photogrammetric

Engineering and Remote Sensing, 65, 289-296.
Hassan, M.M., 1988, Filtering Digital Profile Observations, Photogrammetric Engineering and Remote Sensing, 54 (10), 1391-1394.
Hewson, R.D., Cudahy, T.J., Mizuhiko, S., Ueda, K., and Mauger, A.J., 2005, Seamless Geological Map Generation Using ASTER in the Broken Hill–Curnamona Province of Australia. Remote Sensing of Environment, 99, 159–172.
Hook, S.J., Myers, J.J., Thome, K.J., Fitzgerald, M., Kahle, A.B., 2001, The MODIS/ASTER airborne simulator (MASTER): a new instrument for earth science studies. Remote. Sens. Environ., 76, 93–102.
Hunt, G.R., 1977, Spectral signatures of particulate minerals in the visible and near infrared. Geophysics, 42, 501–513.
Iikura, Y. and Yokoyama, R., 1999, Correction of Atmospheric and Topographic Effects on Landsat TM Imagery, Journal of the Remote Sensing Society of Japan, 19 (1), 2-16.
Iwahashi, J. and Pike, R.J., 2007, Automated classifications of topography from DEMs by an unsupervised nested-means algorithm and a three-part geometric signature. Geomorphology, 86, 409-440.
Japan Oil, Gas and Metals National Corporation (JOGMEC), 2005, Resource development environment research report of the Middle East countries (Iran, Oman, Saudi Arabia, Turkey), pp. 1-64.
John, D.A., Rockwell, B.W., Henry, C.D., Colgan, J.P., 2010, Hydrothermal alteration of the late Eocene Caetano ash-flow caldera, north-central Nevada: a field and ASTER remote sensing study. Geological Society of Nevada 2010 Symposium Volume, Reno, Nevada, May 14–22 2010, 1055–1083.
Kahle, A.B., 1976, Thermal inertia imaging: a new geologic mapping tool. Geophys. Res. Lett., 3, 419–421.
Kahle, A.B., Rowan, L.C., 1980, Evaluation of multispectral middle infrared aircraft images for lithologic mapping in the East TinticMountains, Utah. Geology, 8, 234–239.
Kahle, A.B., Goetz, F.H., 1983, Mineralogic information from a new airborne thermal infrared multispectral scanner. Science, 222, 24–27.
Kahle, A.B., Schieldge, J.P., Alley, R.E., 1984, Sensitivity of thermal inertia calculations to variations in environmental factors. Remote. Sens. Environ., 16, 211–232.
Kruse, F.A., 2002, Comparison of AVIRIS and Hyperion for Hyperspectral Mineral Mapping. 11th JPL Airborne Geoscience Workshop.
Kruse, F.A., Boardman, J.W., and Huntington, J.F., 2003, Comparison of Airborne

Hyperspectral Data and EO-1 Hyperion for Mineral Mapping. IEEE Transactions on Geoscience and Remote Sensing, 41, 1388-1400.

Liang, S., 2000, Narrowband to broadband conversions of land surface albedo I algorithms. Remote. Sens. Environ., 76, 213–238.

Loughlin, W.P., 1991, Principal Component Analysis for Alteration Mapping. Photogrammetric Engineering and Remote Sensing, 57 (9), 1163-1169.

Lyon, R.J.P., Lee, K., 1970, Remote sensing in exploration for mineral deposits. Economic Geology, 65, 785–800.

Lyon, R.J.P., 1972, Infrared spectral emittance in geological mapping: airborne spectrometer data from Pisgah Crater. Science, 7, 983–986.

Machacha, T.P., 1997, The Pre-Kalahari Geological Map of the Republic of Botswana.

Maier, W.D., Barnes, S.J., Chinyepi, G., Barton, J.M., Eglington, B., Setshedi, I., 2008. The composition of magmatic Ni–Cu–(PGE) sulfide deposits in the Tati and Selebi–Phikwe belts of eastern Botswana. Miner. Deposita, 43, 37–60.

Masoud, A. and Koike, K., 2006, Tectonic architecture through Landsat-7 ETM+/SRTM DEM-derived lineaments and relationship to the hydrogeologic setting in Siwa region, NW Egypt. Journal of African Earth Sciences, 45, 467-477.

McCourt, S., Kampunzu, A.B., Bagai, Z., Armstrong, R.A., 2004, The crustal architecture of Archaean terranes in northeastern Botswana. S. Afr. J. Geol., 107, 147–158.

Metal Mining Agency of Japan (MMAJ), Metal Resource Information Center (MRIC), 2003, Resource development environment research report of Iran.

Ministry of Economy Trade and Industry (METI), Metal Mining Agency of Japan (MMAJ), 2000, Spectral database of rocks and minerals.

Naldrett, A.J., 2004, Magmatic Sulfide Deposits: Geology, Geochemistry and Exploration. Springer Verlag.

Naldrett, A.J., 2010, Secular variation of magmatic sulfide deposits and their source magmas. Economic Geology, 105, 669–688.

Ninomiya, Y., Fu, B., Cudahy, T.J., 2005, Detecting lithology with Advanced Spaceborne Thermal Emission and Reflection Radiometer (ASTER)multispectral thermal infrared “radiance-at-sensor” data. Remote. Sens. Environ., 99, 127–139.

Ninomiya, Y., Fu, B., 2010, Regional scale lithologic mapping in western Tibet using ASTER thermal infrared multispectral data. Int. Arch. Photogramm. Remote. Sens. Spat. Inf. Sci., 38, 454–458.

Ono, A., Fujiwara, N. and Ono, A., 2002, Suppression of topographic and atmospheric effects by normalizing the radiation spectrum of Landsat/TM by the sum of each

band, Journal of the Remote Sensing Society of Japan, 22 (3), 318-327.

Oppenheim, A.V. and Schafer, R.W., 1975, Digital Signal Processing. Prentice-Hall, p. 585.

Pan, J.J., 1989, Spectral Analysis and Filtering Techniques in Digital Spatial Data Processing. Photogrammetric Engineering and Remote Sensing, 55, 1203-1207.

Partington, G.A., Williams, P.J., 2000, Proterozoic lode gold and (iron)–copper–gold deposits: a comparison of Australian and global examples. Reviews in Economic Geology, 13, 69–101.

Pratt, D.A., Ellyett, C.D., McLauchlan, E.C., McNabb, P., 1978, Recent advances in the application of thermal infrared scanning to geological and hydrological studies. Remote. Sens. Environ., 7, 177–184.

Price, J.C., 1977, Thermal inertia mapping: a new view of the Earth. J. Geophys. Res., 82 (18), 2582–2590.

Rabus B, Eineder M, and Roth A., 2003, The Shuttle Radar Topography Mission - a New Class of Digital Elevation Models Acquired by Spaceborne Radar. ISPRS Journal of Photogrammetry and Remote Sensing, 57, 241-262.

Rockwell, B.W., Hofstra, A.H., 2008, Identification of quartz and carbonateminerals across northern Nevada using ASTER thermal infrared emissivity data: implications for geologic mapping and mineral resource investigations in well-studied and frontier areas. Geosphere, 4, 218–246.

Rockwell, B.W., 2009, Comparison of ASTER- and AVIRIS-derived mineral and vegetation maps of the White Horse replacement alunite deposit and surrounding area, Marysvale volcanic field, Utah. U.S. Geological Survey Scientific Investigations Report 2009–5117 (31 pp. http://pubs.usgs.gov/sir/2009/5117/).

Rowan, L.C., Hook, S.J., Abrams, M.J., and Mars, J.C., 2003, Mapping Hydrothermally altered rocks at Cuprite, Nevada, using the Advanced Spaceborne Thermal Emission and Reflection Radiometer (ASTER), a new satellite-imaging system. Economic Geology, 98, 1019-1027.

Roy D.P. SAFARI 2000 MODIS 500-m burned area products, Southern Africa, Dry season 2000. Data set 2005. Available on-line [http://daac.ornl.gov/] from Oak Ridge National Laboratory Distributed Active Archive Center, Oak Ridge, Tennessee, USA Data Set Link: http://modis-fire.gsfc.nasa.gov/index.asp.

Sabine, C., Realmuto, V.J., Taranik, J.V., 1994, Quantitative estimation of granitoid composition from thermal infrared multispectral scanner (TIMS) data, desolation wilderness, northern Sierra Nevada, California. J. Geophys. Res., 99 (B3), 4261–4271.

Salisbury, J.W., Walter, L.S., 1989, Thermal infrared (2.5–13.5 μm) spectroscopic remote sensing of igneous rock types on particulate planetary surfaces. J. Geophys. Res., 94 (B7), 9192–9202.

Sillitoe, R.H., 2000, Gold-rich porphyry deposits: Descriptive and genetic models and their role in exploration and discovery, Society of Economic Geology Reviews, 13, 315-345.

Sillitoe, R.H., 2010, Porphyry Copper Systems, Economic Geology, 105, 3-41.

Singh, B. and Dowerah, J., 2010, ASTER DEM Based Studies for Geological Investigation around Singhbhum Shear Zone (SSZ) in Jharkhand, India. Journal of Geographic Information System, 2, 11-14.

Smith, R.A., 1984, The lithostratigraphy of the Karoo Supergroup in Botswana. Bulletin, 26. Geological Survey, Botswana, p. 239.

Smith, M. J. and Clark, C. D., 2005, Methods for the Visualization of Digital Elevation Models for Landform Mapping. Earth Surface Processes and Landforms, 30, 885–900.

Stagman J.G., 1977, Provisional geological map of Rhodesia, 1:1,000,000, Rhodesia Geological Survey.

Tachikawa, T., Hato, M., Kaku, M., and Iwasaki, A., 2011, The Characteristics of ASTER GDEM Version 2. IGARSS 2011 Vancouver, 3657-3661.

Tangestani, M.H. and Moore, F., 2002, Porphyry copper alteration mapping at the Meiduk area, Iran, International Journal of Remote Sensing, 23 (22), 4815-4825.

Taranik, J.V., Coolbaugh, M.F., Vaughan, R.G., 2009, An overview of thermal infrared remote sensing with applications to geothermal andmineral exploration in the Great Basin, Western United States. Reviews in Economic Geology, 16, 41–57.

United States Geological Survey (USGS), 2003, LANDSAT 7 Image Assessment System (IAS) Radiometric Algorithm Theoretical Basis Document (ATBD).

United States Geological Survey (USGS), 2010, Porphyry Copper Deposit Model. Scientific Investigations Report 2010-5070-B, p. 186.

Van Geffen, P.W.G., 2004, Geochemistry of the Phoenix Ni-Cu-PGE deposit, Francistown, Botswana. MSc thesis, Utrecht University, p. 1-88.

Watson, K., 1975, Geological applications of thermal infrared images. Proc. IEEE, 63, 128–137.

Yamaguchi, Y., Kahle, A.B., Tsu, H., Kawakami, T., Pniel, M., 1998, Overview of Advanced Spaceborne Thermal Emission and Reflection Radiometer (ASTER). IEEE Trans. Geosci. Remote Sens., 36, 1062–1071.

## ACKNOWLEDGEMENTS

I would like to express my deepest gratitude to my supervisor, Prof. Yasushi Yamaguchi, for his instruction and continuous encouragement throughout all my doctoral studies in Nagoya University. I greatly appreciate to participate in the study using the ASTER sensor with him because he was involved from the development stage of ASTER and throughout the operation stage to present. ASTER is a sensor that is well designed and makes us proud. His wide knowledge and creative way of thinking have been great value for me, and he also provided his facility and funding to support the whole process of my research and paper publishing. Besides the professional knowledge, I also learned about his kindness in communication and carefulness in work, which I believe will benefit me much in my future career.

Also, I would like to express my appreciation to the members in the lab of earth environmental system for their meaningful suggestions and comments in each seminar. Especially I appreciate Oshigami-san, Uezato-san and Ishidoshiro-san for their helpful support, hospitality and discussions during my study.

Simultaneously, I would like to express my appreciation to my co-workers at JOGMEC (Sakasegawa-san, Moriwaki-san, Ueda-san, Hayashi-san, Suzuki-san, Miyatake-san, Morozumi-san, Arai-san, Takeda-san, Momose-san, Mitsuishi-san, Kondo-san), Sumitomo Metal Mining Co. (Yamamoto-san), Mitsui Mining Co. (Murakami-san). My study could not be accomplished without their support, discussions and comments.

Before last, I would thank my family (wife and sons) for patience, support and encouragement during the long period of my study.

Finally, I would like to thank my Lord and Savior, Jesus Christ, for allowing my life, health, love, salvation, and the chance for finding this study and work that I had found as my interest for living while here on this earth.

Taro YAJIMA
January, 2014